



Topology optimization of shape memory polymer structures with programmable morphology

Anurag Bhattacharyya¹ · Kai A. James¹ Received: 1 January 2020 / Revised: 23 October 2020 / Accepted: 5 November 2020
© Springer-Verlag GmbH Germany, part of Springer Nature 2020

Abstract

We present a novel optimization framework for optimal design of structures exhibiting memory characteristics by incorporating shape memory polymers (SMPs). SMPs are a class of memory materials capable of undergoing and recovering applied deformations. A finite-element analysis incorporating the additive decomposition of small strain is implemented to analyze and predict temperature-dependent memory characteristics of SMPs. The finite element method consists of a viscoelastic material modelling combined with a temperature-dependent strain storage mechanism, giving SMPs their characteristic property. The thermo-mechanical characteristics of SMPs are exploited to actuate structural deflection to enable morphing toward a target shape. A time-dependent adjoint sensitivity formulation implemented through a recursive algorithm is used to calculate the gradients required for the topology optimization algorithm. Multimaterial topology optimization combined with the thermo-mechanical programming cycle is used to optimally distribute the active and passive SMP materials within the design domain. This allows us to tailor the response of the structures to design them with specific target displacements, by exploiting the difference in the glass-transition temperatures of the two SMP materials. Forward analysis and sensitivity calculations are combined in an PETS-based optimization framework to enable efficient multi-functional, multimaterial structural design with controlled deformations.

Keywords Multimaterial topology optimization · Shape memory polymers · Multi-physics design · Adjoint sensitivity analysis · High-performance computing

1 Introduction

Nature has always been a source of inspiration to push forward the frontiers of science and technology. One of the complex and interesting phenomena which has widely been mimicked is the shape changing or morphing phenomenon (Siéfert et al. 2019; Oliver et al. 2016). From an aerospace engineering point of view, the concept of morphing has gained momentum because of its potential to push the limits of the current flight technologies and make them more efficient. A wide range of smart materials capable of producing structural morphing has been studied and many

more are currently under investigation. Shape memory materials have shown promising results in this respect.

Shape memory materials (SMM) are materials capable of recovering their original shape in the presence of the right stimulus after being quasi-plastically deformed. Two widely known types of SMMs are shape memory alloys (SMA) and shape memory polymers (SMPs). From an engineering perspective, tailoring the shape and other properties of polymers is much easier as compared to metals. This, along with other advantages mentioned in later paragraphs, motivated the current research to computationally design structures using SMPs to tailor their motion to fulfil specific design objectives.

Shape memory polymers are a class of multi-phase materials which have the ability to regain their original (permanent) shape from a deformed shape (temporary shape) as a result of a shape memory recovery process. The shape memory recovery process can be induced by a variety of stimuli like heat, light, electricity, or magnetism. The main advantages of SMPs compared to metallic shape memory alloys are substantially higher elongations,

Responsible Editor: Seonho Cho

✉ Anurag Bhattacharyya
bhattachr6@illinois.edu

¹ University of Illinois Urbana-Champaign, Urbana, IL 61801, USA

32 lower density, biodegradability, and the ability to be
 33 easily manufactured and given complex shapes through 3D
 34 printing technology. All these factors have made SMPs
 35 widely used in variety of applications, and particularly
 36 suited for aerospace applications (Behl and Lendlein 2011).

37 SMPs have been successfully used in developing self-
 38 deploying sun-rails or antennas for spacecrafts and satellites
 39 (Liu et al. 2014). The deployable panels are connected
 40 to SMP hinges that are deformed when storage and
 41 transportation are required but when exposed to heat they
 42 come back to their original undeformed state, thereby
 43 deploying the panels. SMP composites have also been
 44 investigated for wing morphing applications (Reed et al.
 45 2005; Leng et al. 2010; Yu et al. 2009). Wache et
 46 al. prototyped and tested SMP stents using the natural
 47 body temperature for activation (Wache et al. 2003).
 48 Reconfigurable drug-delivery devices made of SMPs,
 49 capable of self-assembling, have also been studied (Cho
 50 et al. 2010). Heat-triggered movements of SMPs were
 51 also investigated to design snap-fit mechanisms to allow
 52 for easier disassembly in the production/packaging sector
 53 (Carrell et al. 2011).

54 A variety of experimental and constitutive modelling
 55 techniques for SMPs have already been investigated to
 56 better understand the thermo-mechanical characteristics of
 57 SMPs. Due to a growing interest in SMPs, a lot of
 58 experimental work to characterize their behavior has been
 59 carried out (Liu et al. 2006; Lendlein et al. 2005; Volk
 60 et al. 2011). Simultaneously, development of constitutive
 61 modelling techniques to predict and describe SMP behavior
 62 accurately has also been extensively investigated (Qi et al.
 63 2008; Chen and Lagoudas 2008a, b; Baghani et al. 2012;
 64 Reese et al. 2010). Studies have been carried out to combine
 65 SMP modelling techniques with 4D printing to design active
 66 origami structures which can morph into specific target
 67 shapes (Ge et al. 2016; Tibbitts 2014).

68 The potential of SMPs can be exploited to design
 69 morphing structures with specific tailored output motion
 70 through computational design techniques. Isogeometric
 71 configuration design optimization has been investigated
 72 to synthesize lattice structures with SMPs (Choi and
 73 Cho 2018). Topology optimization techniques have also
 74 been implemented to design multimaterial non-intuitive
 75 structures with specific objective functions for different
 76 material models (Bendsøe and Sigmund 1999; James
 77 and Waisman 2015; Carbonari et al. 2008; Gaynor
 78 et al. 2014). It has been successfully investigated to
 79 design structures with SMAs and other smart materials
 80 with multi-physics characteristics (Sigmund and Torquato
 81 1999; Frecker 2003; Silva and Kikuchi 1999; Bowen
 82 et al. 2014; Rupp et al. 2009; Yin and Ananthasuresh
 83 2002; Langelaar and van Keulen 2008; Langelaar et al.
 84 2011). Level-set topology optimization has been utilized

85 to design morphing structures with active materials and
 86 to determine the material interfaces in printed active
 87 composites (PACs) consisting of SMPs (Maute et al. 1402).
 88 Recent studies have also explored the use of the extended
 89 finite element method (XFEM) combined with the level-set
 90 method to design self-actuating, shape-changing structures,
 91 capable of undergoing large deformations (Geiss and Maute
 92 2018; Geiss et al. 2019). This approach enables explicit
 93 representation of the material boundary to better exploit
 94 emerging additive manufacturing technologies. The current
 95 study aims to further expand the scope of the application
 96 of topology optimization framework to design morphing
 97 structures through continuous distribution of multiple SMP
 98 materials throughout the design domain to be able to design
 99 mechanisms and multi-functional structures with complex
 100 motions.

101 This paper proposes a novel optimization framework to
 102 harness the potential of SMPs to design structures with
 103 specific target displacements via topology optimization.
 104 The multi-physics SMP behavior has been simulated using
 105 MATLAB- and PETSc-based implementations. The current
 106 study includes a unique attempt to implement a time-
 107 dependent adjoint sensitivity analysis for SMP structures,
 108 and uses the gradient information to computationally design
 109 shape-changing structures through topology optimization.
 110 We propose a novel, computationally efficient, thermo-
 111 mechanical programming cycle for SMPs, and using
 112 this technique several multimaterial topology optimization
 113 designs for morphing structures are presented.

2 Thermo-mechanical programming cycle

114 The SMP mechanics are governed by the characteristics
 115 of its constituent phases namely a rubbery phase and a
 116

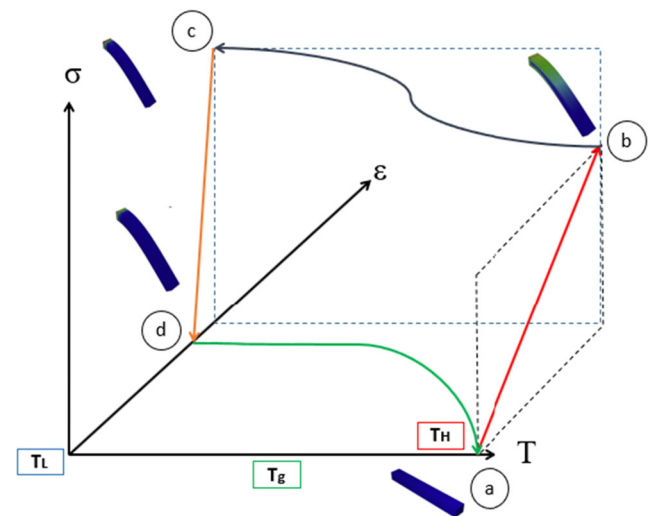


Fig. 1 Thermo-mechanical programming cycle for SMPs

117 glassy phase. The thermo-mechanical programming cycle is
 118 responsible for making SMPs exhibit their shape memory
 119 characteristics. When the temperature during the thermo-
 120 mechanical cycle changes from the maximum temperature
 121 (T_H) to the minimum temperature (T_L), the volume fraction
 122 of the rubbery and glassy phases changes, changing
 123 the structural behavior of the polymer and imparting it
 124 with memory characteristics. Figure 1 shows the thermo-
 125 mechanical cycle for programming SMPs on a stress (σ)-
 126 strain (ϵ)-temperature (T) axis frame. Initially, the structure
 127 is in state (a) at the maximum temperature (T_H) where the
 128 material is primarily in the rubbery phase. Then, keeping
 129 the temperature constant, it is deformed from state (a) to
 130 state (b). After being deformed to the required shape, the
 131 strain is kept constant and the temperature is decreased
 132 from T_H to T_L . As the temperature is reduced, the internal
 133 stress increases from state (b) to state (c). While going
 134 from T_H to T_L , the structure passes through the *glass*
 135 *transition* temperature (T_g). Before reaching T_g , most of
 136 the polymer is in the rubbery phase and after crossing T_g
 137 most of the material switches to a glassy phase which has
 138 higher stiffness than the rubbery phase. At state (c), the
 139 external applied forces are removed and the material is
 140 allowed to relax, during which time the internal stresses
 141 reduce to 0 at state (d). State (d) is the temporary shape of
 142 the structure and it can stay in this state until heated. Finally,
 143 the structure is heated back to T_H after which it regains
 144 its original undeformed shape (a). Since the recovery of
 145 its original undeformed configuration happens with the no
 146 internal stresses, this cycle is called the *stress free strain*
 147 *recovery* cycle.

3 Small-strain finite element analysis

149 The FEA model implemented in this study is based on
 150 the SMP small-strain constitutive model as proposed by
 151 Baghani et al. (2012). In this algorithmic implementation,
 152 we have not considered geometric nonlinearity.

Using the concept of additive decomposition of small
 153 strains, the total strain, ϵ , can be split into components as: 154

$$\epsilon = \phi^g \epsilon^g + \phi^r \epsilon^r + \epsilon^i + \epsilon^T + \epsilon^{is} \tag{1}$$

Here, ϕ^g and ϕ^r refer to the glassy-phase volume fraction
 155 and rubbery-phase volume fraction, respectively. The
 156 volume fractions of the rubbery phase (ϕ^r) and the glassy
 157 phase (ϕ^g) are related by: 158

$$\phi^g + \phi^r = 1 \tag{2}$$

Terms ϵ^g , ϵ^r , ϵ^i , ϵ^T , and ϵ^{is} in the rheological model shown
 159 in Fig. 2 refer to the glassy-phase strain, strain in the rubbery
 160 phase, the inelastic strain component, the thermal strain, and
 161 the stored strain. The strain in the rubbery (ϵ^r) and glassy
 162 (ϵ^g) phases can be further spilt into the inelastic and elastic
 163 strain components as shown below. 164

$$\begin{aligned} \epsilon^r &= \epsilon^{er} + \epsilon^{ir} \\ \epsilon^g &= \epsilon^{eg} + \epsilon^{ig} \end{aligned} \tag{3}$$

The time-continuous inelastic strain evolution equations are
 165 defined by: 166

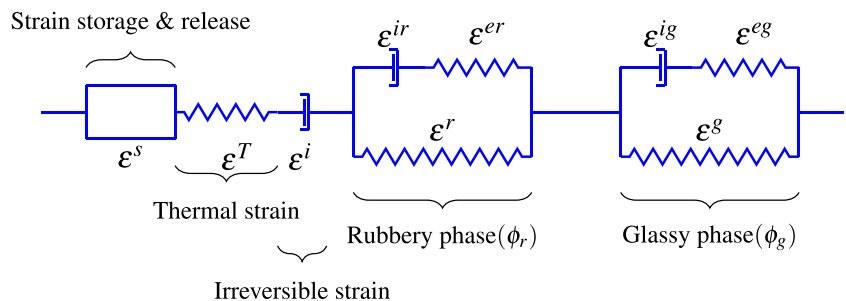
$$\begin{aligned} \dot{\epsilon}^{ir} &= \frac{\mathbb{K}_r^{neq}}{\eta_r} : (\epsilon^r - \epsilon^{ir}) \\ \dot{\epsilon}^{ig} &= \frac{\mathbb{K}_g^{neq}}{\eta_g} : (\epsilon^g - \epsilon^{ig}) \\ \dot{\epsilon}^i &= \frac{1}{\eta_i} \sigma \end{aligned} \tag{4}$$

Here, \mathbb{K}^{neq} represents the stiffness contribution of the non-
 167 equilibrium branch of the respective phases, η refers to the
 168 viscosity coefficient of the phases, and σ refers to the total
 169 internal stress. 170

The evolution equations describing the stored strain
 171 components are defined by: 172

$$\begin{aligned} \dot{\epsilon}^{is} &= \dot{\phi}^g \epsilon^r \text{ Cooling phase} \\ \dot{\epsilon}^{is} &= \dot{\phi}^g \frac{\epsilon^{is}}{\phi^g} \text{ Heating phase} \end{aligned} \tag{5}$$

Fig. 2 The rheological model of shape memory polymer



173 In the constitutive modelling and verification, as provided in
 174 [Appendix](#) section, of a single SMP material, the evolution
 175 of the volume fraction of the glassy phase is given by:

$$\phi_g = 1 - \frac{1}{1 + 2.76 \times 10^{-5}(T_{max} - T)^4} \quad (6)$$

176 Here, T_{max} is the maximum temperature of the thermo-
 177 mechanical programming cycle and T is the temperature dur-
 178 ing any step of the thermo-mechanical process. For two SMP
 179 material topology optimization algorithm, since the materials
 180 have different glass-transition temperatures (T_g), the vol-
 181 ume fraction of the second SMP material is calculated by:
 182

$$\phi_g = 1 - \frac{1}{1 + \exp(-0.66(T - T_g))} \quad (7)$$

183 The thermal strains in the structure are calculated by:

$$\boldsymbol{\epsilon}^T = (\alpha_1(T - T_h) + \alpha_2(T^2 - T_h^2))\mathbf{1} \quad (8)$$

184 Here, α_1 and α_2 for a two-material topology optimization
 185 formulation are given in [Table 1](#). The term $\mathbf{1}$ denotes the iden-
 186 tity tensor. The evolution equations are converted from a
 187 time-continuous form to discrete time-stepping equations by
 188 applying a backward-Euler differencing scheme. As a result
 189 of this conversion, the evolution equations can be defined
 190 as:

$$\begin{aligned} \boldsymbol{\epsilon}_n^{ir} &= \mathbb{H}_r^{-1} : \boldsymbol{\epsilon}_{n-1}^{ir} + \mathbb{W}_r : \boldsymbol{\epsilon}_n^r \\ \boldsymbol{\epsilon}_n^{ig} &= \mathbb{H}_g^{-1} : \boldsymbol{\epsilon}_{n-1}^{ig} + \mathbb{W}_g : \boldsymbol{\epsilon}_n^g \\ \boldsymbol{\epsilon}_n^i &= \boldsymbol{\epsilon}_{n-1}^i + \mathbb{M} : \boldsymbol{\epsilon}_n^r - \mathbb{N} : \boldsymbol{\epsilon}_{n-1}^{ir} \\ \boldsymbol{\epsilon}_n^{is} &= \boldsymbol{\epsilon}_{n-1}^{is} + \mathbb{P} : \boldsymbol{\epsilon}_n^r \\ \boldsymbol{\epsilon}_n^g &= \mathbb{O} : \boldsymbol{\epsilon}_n^r + \mathbb{E} : \boldsymbol{\epsilon}_{n-1}^{ir} + \mathbb{F} : \boldsymbol{\epsilon}_{n-1}^{ig} \end{aligned} \quad (9)$$

191 where the terms \mathbb{W}_r , \mathbb{W}_g , \mathbb{M} , \mathbb{N} , \mathbb{P} , \mathbb{H}_r , \mathbb{H}_g , \mathbb{O} , \mathbb{E} , and \mathbb{F}
 192 are defined in [\(A.2\)](#) and [\(A.1\)](#). In the derivation of [\(9\)](#), it
 193 has been assumed that the stresses in the glassy and rubbery
 194 phases are equal. The subscript, n , represents the time step.
 195 The total strain in the rubbery phase can be calculated by:

$$\boldsymbol{\epsilon}_{n+1}^r = \mathbb{D}_{n+1}^{-1} : \mathbf{C}_{n+1} \quad (10)$$

Table 1 Values of material properties

$\eta_i^{SMP^1}, \eta_i^{SMP^2}$	10,000, 15,000	MPa·min
$\eta_r^{SMP^1}, \eta_r^{SMP^2}$	1, 1.5	MPa·min
$\eta_g^{SMP^1}, \eta_g^{SMP^2}$	4000, 4500	MPa·min
$\nu_r^{SMP^1}, \nu_g^{SMP^2}$	0.4, 0.4	[-]
$\nu_g^{SMP^1}, \nu_g^{SMP^2}$	0.3, 0.3	[-]
$E_{eq}^{r SMP^1}, E_{eq}^{r SMP^2}$	0.39, 0.5	MPa
$E_{eq}^g SMP^1, E_{eq}^g SMP^2$	1100, 1500	MPa
$E_{neq}^{r SMP^1}, E_{neq}^{r SMP^2}$	0.02, 0.04	MPa
$E_{neq}^g SMP^1, E_{neq}^g SMP^2$	150, 180	MPa
$\alpha_1^{SMP^1}, \alpha_1^{SMP^2}$	$-3.14 \times 10^{-4}, -3.14 \times 10^{-6}$	K^{-1}
$\alpha_2^{SMP^1}, \alpha_2^{SMP^2}$	$0.7 \times 10^{-6}, 0.7 \times 10^{-10}$	K^{-2}

where the terms \mathbb{D}_{n+1} and \mathbf{C}_{n+1} are evaluated using:

$$\begin{aligned} \mathbb{D}_{n+1} &= (\phi_{n+1}^r + \Delta\phi_{n+1}^g)\mathbb{I} + \phi_{n+1}^g(\mathbb{A}_g^{-1}\mathbb{A}_r) + \frac{\Delta t}{\eta_i}\mathbb{A}_r \\ \mathbf{C}_{n+1} &= \boldsymbol{\epsilon}_{n+1} + \phi_{n+1}^g \left[\mathbb{A}_g^{-1} : \{-\mathbb{B}_r : \boldsymbol{\epsilon}_n^{ir} + \mathbb{B}_g : \boldsymbol{\epsilon}_n^{ig}\} \right] \\ &\quad - \boldsymbol{\epsilon}_n^i + \frac{\Delta t}{\eta_i}\mathbb{B}_r : \boldsymbol{\epsilon}_n^{ir} - \boldsymbol{\epsilon}_n^{is} - \boldsymbol{\epsilon}_{n+1}^T \end{aligned} \quad (11)$$

where the terms \mathbb{A}_r , \mathbb{A}_g , \mathbb{B}_r , \mathbb{B}_g and $\Delta\phi_{n+1}^g$ are defined in
[\(A.1\)](#). The total internal stress and the tangent stiffness
matrix are computed as:

$$\boldsymbol{\sigma}_{n+1} = \mathbb{A}_r : \boldsymbol{\epsilon}_{n+1}^r - \mathbb{B}_r : \boldsymbol{\epsilon}_n^{ir} \quad (12)$$

$$\mathbb{C}_{n+1}^{tan} = \mathbb{A}_r \mathbb{D}_{n+1}^{-1} \quad (13)$$

The residual vector \mathbf{R}_{n+1} can be defined as:

$$\mathbf{R}_{n+1} = \mathbf{F}_{n+1}^{int} - \mathbf{F}_{n+1}^{ext} \quad (14)$$

$$\mathbf{F}^{int} = \int_{\Omega} \mathbf{B} \boldsymbol{\sigma}_{n+1} dv \quad (15)$$

where Ω refers to the whole structural domain, and \mathbf{F}_{n+1}^{ext} is
the total external force applied to the structure. The term \mathbf{B}
represents the strain-displacement matrix.

The constitutive model was implemented in a PETSc-
based finite-element framework to perform structural
optimization with a large number of design variables. Note
that in this implementation of the constitutive model, we
have assumed a uniform temperature field throughout the
heating and cooling processes. This assumption reflects
the slow temperature change during the thermomechanical
programming cycle, and it enables us to avoid solving the
coupled thermal conduction problem. Thus, at each step of
the simulation, we effectively solve:

$$\nabla \cdot \boldsymbol{\sigma}_n(T_n, \mathbf{x}) = 0 \quad (16)$$

where T_n is the temperature at time-step t_n and \mathbf{x} refers to
the position of a particular point in the design domain. The
verification of the implementation of the constitutive model
has been provided in the [Appendix](#) section.

4 Topology optimization

4.1 A two-material approach for SMP structural design using a modified thermo-mechanical cycle

To produce morphing shape memory polymer structures, a
design approach utilizing two SMP materials with different
glass-transition temperatures is used. The SMP material
with the lower glass-transition temperature is hereafter
referred to as the *active* SMP material and the SMP material
with the higher glass-transition temperature is referred
to as the *passive* SMP material. The idea is to use the

229 difference in the glass-transition temperature of the two
 230 SMP materials as a driving stimulus to deform the whole
 231 structure toward a specific target shape. The difference
 232 in the glass-transition temperatures would manifest as a
 233 difference in the amount of rubbery and glassy phases in the
 234 active and passive SMP materials. For a nominal amount
 235 of axial deformation, applied during the deformation step
 236 of the thermo-mechanical programming cycle, the two SMP
 237 materials will deform by different amounts, during the
 238 heating phase of the thermo-mechanical cycle, leading to
 239 the bending of the entire structure. The goal of the topology
 240 optimization algorithm is to select the distribution of the
 241 active and passive SMP materials throughout the design
 242 domain such that the deformation of the structure can be
 243 controlled to achieve specific displacements.

244 Due to high computational costs of the entire sensitivity
 245 analysis formulation as explained in the previous section,
 246 the thermo-mechanical cycle was shortened while preserv-
 247 ing its essential components required for imparting shape
 248 memory characteristics to the SMP. The modified SMP
 249 programming cycle for two-material topology optimization
 250 is shown in Fig. 3. The maximum temperature (T_H) and
 251 the minimum temperature (T_L) are chosen to be 350 K
 252 and 330 K, respectively. The *glass transition temperature*
 253 (T_g^a) for the active SMP material is 340 K while that of
 254 the passive SMP material (T_g^p) is 345 K. The transition
 255 temperatures chosen here are similar to the temperatures
 256 used in SMP experimental and computational studies as
 257 provided by Baghani et al. (2012). The minimum tempera-
 258 ture has been chosen to be 330 K to keep the temperature

range small, while allowing for the full spectrum of material
 phases, in order to keep computational costs reasonable.

Instead of deforming the structure at T_H and then
 cooling while keeping the strains constant, the cooling and
 deformation of the structure were done simultaneously. The
 heating and cooling rate used is ± 1 K/min. This reduced
 the requirement for modelling the entire thermo-mechanical
 cycle but at the same time kept the essential parts of the
 cycle to be able to successfully computationally design SMP
 structures with specific objectives.

The SMP thermo-mechanical programming cycle used
 for the numerical case studies is as follows:

- Step I: The temperature is decreased from T_H to T_L
 while deforming the structure with a constant load F for
 a total time of 20 min simulated with 4 time steps. This
 step is indicated with the label “C+D” in Fig. 3.
- Step II: The structure is allowed to relax without any
 external forces for a total time of 15 min simulated with
 3 time steps. This is labeled “R” in Fig. 3.
- Step III: The structure is heated from T_L to T_g^a over
 a duration of 10 min simulated with 2 time steps. This
 step is labeled “H” in Fig. 3.

During step III of the thermo-mechanical cycle, the structure
 is heated to a temperature of T_g^a , which corresponds to
 the glass-transition temperature of the active material. This
 temperature will be represented as T^* for the remainder of
 the paper. This results in a very high volume fraction of the
 glass phase in the *passive* SMP material while the glass-
 phase volume fraction in the active SMP material becomes
 considerably lower. In this way, we have selectively
activated the shape memory response in the active material.
 Consequently, the active material naturally wants to return
 to its default shape, while the passive material wants to
 remain in its temporary shape. This results in an internal
 residual stress that can be optimally harnessed to produce
 complex motion that is effectively programmed into the
 material distribution.

4.2 Design parameterization

The main goal of topology optimization is to determine the
 optimal distribution of a given amount of material inside
 a design domain in such a way that a given objective
 is optimized and constraints are satisfied. To determine
 the optimal material distribution, finite element analysis
 is carried out combined with a SIMP (*solid isotropic
 material penalization*) scheme for material parameter
 interpolation. According to the SIMP formulation for a two-
 material interpolation (without void), the effective material
 properties for each element are evaluated as:

$$\Psi_{eff} = \Psi_1 + \rho^p(\Psi_2 - \Psi_1) \tag{17}$$

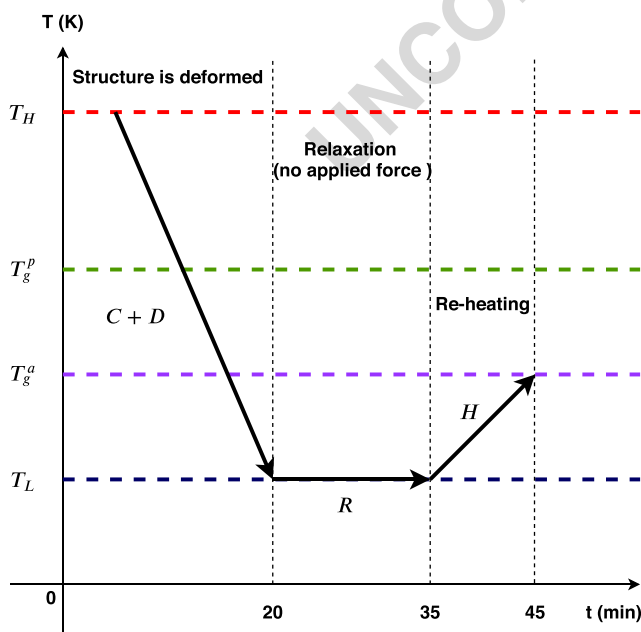
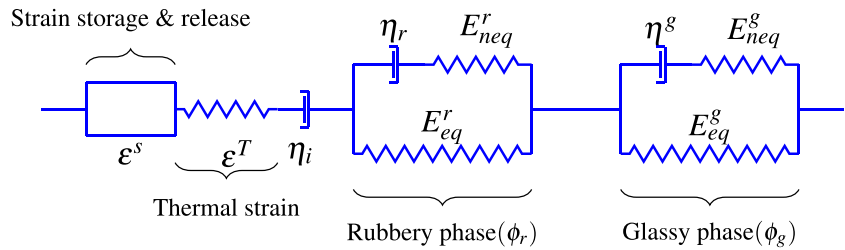


Fig. 3 Modified thermo-mechanical SMP programming cycle

Fig. 4 Rheological model illustrating the physical significance of the SMP material properties



307 Here, Ψ represents a generic material parameter, ρ is the
 308 mixing ratio which ranges from 0 to 1, and p represents the
 309 penalization constant. Generally, p is chosen to be a number
 310 greater than 1 to ensure that the intermediate densities are
 311 penalized and removed from the optimal design. To avoid
 312 mesh dependency and other numerical instabilities resulting
 313 from the topology optimization method, we implement
 314 a density filtering technique as proposed by Bruns and
 315 Tortorelli (2001).

316 For an SMP based on the material properties as shown
 317 in Fig. 4, the SIMP formulation is used to interpolate the
 318 materials' parameters between two SMP materials, SMP^1
 319 and SMP^2 , as explained above. Equation (18) shows the
 320 SIMP interpolation scheme, modified for the two-material
 321 topology optimization framework. We investigate values
 322 of $p = 3$ and $p = 1$ for the penalization constant in
 323 the SIMP scheme of the topology optimization framework.
 324 It can be observed that only the stiffness parameters of
 325 the materials are penalized, and the other properties like
 326 viscosity coefficients (η_r, η_g) and the thermal expansion
 327 coefficients (α_1, α_2) are not penalized. This is done to guide
 328 the optimizer toward a binary solution, in which all elements
 329 exclusively contain one of the two design materials with no
 330 mixing. Table 1 lists the values of the material properties for
 331 the two SMP materials. For all the numerical examples, the
 332 convergence is based on the criterion of $|x_{k+1} - x_k| < 0.01$
 333 as implemented in Aage et al. (2015).

$$\begin{aligned}
 \eta_i &= \eta_i^{SMP^1} + \rho(\eta_i^{SMP^2} - \eta_i^{SMP^1}) \\
 E_{eq}^r &= E_{eq}^{r, SMP^1} + \rho^p(E_{eq}^{r, SMP^2} - E_{eq}^{r, SMP^1}) \\
 E_{neq}^r &= E_{neq}^{r, SMP^1} + \rho^p(E_{neq}^{r, SMP^2} - E_{neq}^{r, SMP^1}) \\
 E_{eq}^g &= E_{eq}^{g, SMP^1} + \rho^p(E_{eq}^{g, SMP^2} - E_{eq}^{g, SMP^1}) \\
 E_{neq}^g &= E_{neq}^{g, SMP^1} + \rho^p(E_{neq}^{g, SMP^2} - E_{neq}^{g, SMP^1}) \\
 \eta_r &= \eta_r^{SMP^1} + \rho(\eta_r^{SMP^2} - \eta_r^{SMP^1}) \\
 \eta_g &= \eta_g^{SMP^1} + \rho(\eta_g^{SMP^2} - \eta_g^{SMP^1}) \\
 \alpha_1 &= \alpha_1^{SMP^1} + \rho(\alpha_1^{SMP^2} - \alpha_1^{SMP^1}) \\
 \alpha_2 &= \alpha_2^{SMP^1} + \rho(\alpha_2^{SMP^2} - \alpha_2^{SMP^1})
 \end{aligned}
 \tag{18}$$

5 Time-dependent adjoint sensitivity analysis

334 Time-dependent adjoint sensitivity analysis is performed to
 335 calculate the gradient information required for the structural
 336 optimization process. The procedure here describes the
 337 calculation of adjoint sensitivities. The function of interest
 338 being differentiated is the displacement at a particular
 339 degree-of-freedom (a) of the structure, at a particular time
 340 step (M) as shown in Fig. 5.

Let the scalar function of interest (θ) be defined as:

$$\theta = \mathbf{u}_a^M(\rho) \tag{19}$$

Let $\mathbf{u}^M(\rho)$ represent the displacement vector of the whole structure at time step M . Then, we can write (19) as:

$$\theta = \mathbf{L}^T \mathbf{u}^M(\rho) \tag{20}$$

where \mathbf{L} is a column vector and is zero everywhere except at the entry corresponding to the a^{th} degree-of-freedom. We can form an augmented Lagrangian function as:

$$\Theta = \theta + \sum_{i=1}^M \left[\lambda^{(i)T} \mathbf{R}^{(i)}(\rho, \mathbf{u}^i, \mathbf{u}^{i-1}, \dots, \mathbf{u}^0) \right] \tag{21}$$

where ρ is the design variable and the variable \mathbf{u} is the state variable (containing all the variables evaluated through forward analysis). Note that $\Theta = \theta$ since $\mathbf{R}^{(i)} = 0$ for all

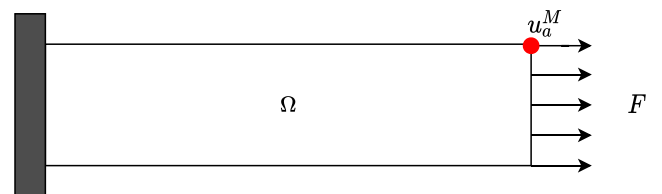


Fig. 5 Design domain for sensitivity calculations and its verification

352 i. Therefore, $\frac{d\Theta}{d\rho} = \frac{d\theta}{d\rho}$. Differentiating (21) with respect to
 353 the design variable ρ , we obtain:

$$\frac{d\Theta}{d\rho} = L^T \frac{d\mathbf{u}^M}{d\rho} + \sum_{i=1}^M \left[\lambda^{(i)T} \left(\sum_{k=1}^i \frac{\partial \mathbf{R}^{(i)}}{\partial \mathbf{u}^{(k)}} \frac{d\mathbf{u}^{(k)}}{d\rho} + \frac{\partial \mathbf{R}^{(i)}}{\partial \rho} \right) \right] \quad (22)$$

354 Expanding the right-hand side terms yields:

$$\begin{aligned} \frac{d\Theta}{d\rho} = & L^T \frac{d\mathbf{u}^M}{d\rho} + \sum_{i=1}^M \lambda^{(i)T} \frac{\partial \mathbf{R}^{(i)}}{\partial \rho} + \lambda^{(M)T} \left(\frac{\partial \mathbf{R}^{(M)}}{\partial \mathbf{u}^{(M)}} \frac{d\mathbf{u}^{(M)}}{d\rho} \right) \\ & + \sum_{i=1}^{M-1} \sum_{k=i}^M \left(\lambda^{(k)T} \frac{\partial \mathbf{R}^{(k)}}{\partial \mathbf{u}^{(i)}} \right) \frac{d\mathbf{u}^{(i)}}{d\rho} \end{aligned} \quad (23)$$

The solution of $\{\lambda^i\}$ which causes all the implicit terms, $\left\{ \frac{d\mathbf{u}}{d\rho} \right\}^1$ to vanish is given by:

$$\begin{aligned} \lambda^{(M)} &= -L^T \left[\frac{\partial \mathbf{R}^{(M)}}{\partial \mathbf{u}^{(M)}} \right]^{-1} \\ \lambda^{(i)} &= - \left[\sum_{k=i+1}^M \lambda^{(k)T} \frac{\partial \mathbf{R}^{(k)}}{\partial \mathbf{u}^{(i)}} \right] \left[\frac{\partial \mathbf{R}^{(i)}}{\partial \mathbf{u}^{(i)}} \right]^{-1} \end{aligned} \quad (24)$$

When solved in this way, the parameters $\{\lambda^i\}$ are referred to as the *adjoint* vectors, and each vector λ^i represents the adjoint state at each time step t_i . Algorithm 1 contains a pseudocode description of the algorithm used to compute the sensitivities of the SMP material.

Algorithm 1 Time-dependent adjoint sensitivity analysis algorithm.

```

df/dρ ← ∂/∂ρ [f(ρ, u(M))] /* initialize sensitivities */
λ(M) ← [∂R(M)/u(M)]-1 [-∂f/u(M)] /* solve for final adjoint state */
for i ← M, M - 1, ..., 0 do
    /* cycle back through each time step */
    FRHS ← 0;
    /* Cycle forward through all subsequent time steps */
    for k ← i + 1, i + 2, M do
        ∂R(k)/∂u(i) ← ∂eir/(i) + ∂eig/(i) + ∂eis/(i) + ∂eis/(i);
        /* Each additive term is traced back in time through
           the recursive Algorithms 2 and 3 */
        FRHS ← FRHS - [λ(k) ∂R(k)/∂u(i)]
    λ(i) ← -FRHS [∂R(i)/∂u(i)]-1 /* solve for intermediate adjoint
       vectors (24) */
    df/dρ ← df/dρ + λ(i) ∂R(i)/∂ρ
    
```

362 Once we obtain the full set of *adjoint* vectors, the
 363 sensitivities can be obtained as:

$$\frac{d\Theta}{d\rho} = \sum_{i=0}^M \lambda^i \frac{\partial \mathbf{R}^i}{\partial \rho} \quad (25)$$

6 Numerical results

6.1 Self-actuating beam

366 The first case study discusses the design of an SMP-based
 367 self-actuating cantilever beam which, when subjected to a
 368 uniaxial load, exhibits a non-axial bending deformation.
 369 The initial design domain along with the boundary and
 370 loading conditions are shown in Fig. 6. The structure is fixed
 371 at one end while a constant uni-axial force (F) is applied at

the other end while decreasing the temperature from T_H to T_L . The objective is to tailor the material distribution inside the design domain such that the displacement in y-direction at a particular node, U_y^N , is maximized at the end of the step III of the thermomechanical cycle when the domain is heated from T_L to T^* , while constraining the total amount of the SMP^1 material used. Mathematically, the optimization problem can be formulated as:

$$\begin{aligned} \text{minimize} \quad & -U_y^N|_{T=T^*} \\ \text{subject to} \quad & V_{SMP^1}(\rho) \leq V_{SMP^1}^{Max}, \quad 0 \leq \rho \leq 1 \end{aligned} \quad (26)$$

¹Note that implicit derivatives, $\frac{d^*}{d\rho}$, capture implicit dependence of a function or state variable with respect to ρ due to the solution of the residual, whereas explicit derivatives capture only direct dependence. Consequently, implicit derivatives are more expensive to evaluate, and therefore we seek to eliminate them from the sensitivity calculation

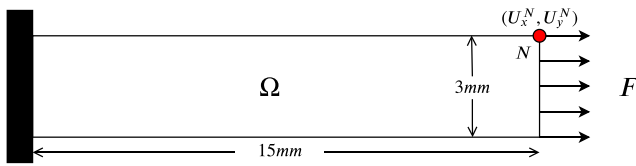


Fig. 6 Initial design domain with boundary conditions and loading conditions

380 Here, T^* represents the time at the end of step III. The term
 381 V_{SMP^1} represents the volume fraction of SMP material of
 382 type 1, represented by SMP^1 , used by the algorithm. It is
 383 defined as:

$$V_{SMP^1} = \frac{\sum_{i=1}^{ne} (1 - \rho_i) v^i}{\sum_{i=1}^{ne} v^i} \quad (27)$$

384 where the elemental design variable ρ_i is defined as:

$$\rho_i = \frac{v_{SMP^2}^i}{v^i} \quad (28)$$

385 where v^i is the total volume of an element. The term $V_{SMP^1}^{Max}$
 386 is the maximum allowable volume fraction of SMP^1
 387 material which is set to 0.7 in this implementation.

388 The design domain selected has a length of 15 mm, a height
 389 of 3 mm, and a thickness of 1 mm. The initial design domain
 390 is meshed with 120×24 linear quadrilateral elements.
 391 The SMP thermo-mechanical cycle is applied as described
 392 above. The optimized design is shown in Fig. 7 for a load
 393 of $F = 0.01$ N applied during step I. In the optimized
 394 design shown in Fig. 7, we can observe that the SMP^1
 395 material with the lower glass-transition temperature is
 396 mostly concentrated along the upper surface of the beam
 397 while the SMP material with the higher glass-transition
 398 temperature is primarily distributed toward the base and
 399 the free edges the design domain. This can be explained
 400 by the fact that at the end of step III, as the temperature
 401 reaches T^* , the SMP^2 material has a considerably higher
 402 volume fraction of glass phase as compared to SMP^1 , due
 403 to which the upper surface wants to retract back to its
 404 original length but this movement is restricted by the SMP^2
 405 material resulting in an upward deflection of the structure as
 406 shown in Fig. 8.





Legend
 $SMP^2(T_g = 345 K)$
 $SMP^1(T_g = 340 K)$

Fig. 7 Optimized material distribution for design of the beam

Keeping the optimized distribution of the two SMP 407
 materials the same inside the design domain, Fig. 8 shows 408
 the deformation of the structure due to different loading 409
 values applied during step I. 410

Figure 8 compares the maximum deflection of the self- 411
 actuating beam for different values of F applied during the 412
 step I of the thermo-mechanical programming cycle. The 413
 initial design domain is shown by the blue dashed lines 414
 in Fig. 8. The maximum displacement in the y -direction, 415
 U_y^N , for a value of $F = 0.01$ N, shown in Fig. 8a, is of 416
 magnitude 0.5567 mm. The initial design domain (shown 417
 with a dashed line) and the beam deformation corresponding 418
 to $F = 0.05$ N are shown in Fig. 8b for which the value of 419
 U_y^N is 2.6531 mm. 420

Figure 15 shows the finite element meshes at different 421
 stages of the applied thermo-mechanical cycle for $F = 0.05$ 422
 N. The beam design for a mesh size of 120×24 took over 423
 64,627 core-hours on 144 processors and 340 optimization 424
 iterations to converge to the above design. 425

The optimization convergence history of the objective 426
 and constraint functions for the design of the self-actuating 427
 beam is shown in Fig. 10. 428

The result shown in Fig. 7 contains visible regions of inter- 429
 mediate material, whose properties are a combination of 430
 SMP^1 and SMP^2 . Because the design problem does not 431
 prioritize stiffness, these regions are not deemed inefficient 432
 from the standpoint of the optimizer. Measures could be 433
 taken to suppress the presence of these regions (potentially 434
 sacrificing some degree of performance). However, we have 435
 not pursued these measures, since the intermediate materials 436
 do not hinder the manufacturability of the design. Indeed, 437
 current 3D printing technology for shape memory polymers 438
 allows us to generate *digital* hybrid materials, whose mate- 439
 rial properties are an interpolation of two baseline materials 440
 (Ge et al. 2014). 441

Figure 11 shows the optimized material distribution for 442
 the design of the self-actuating beam with penalization 443
 parameter $p = 1$. The maximum displacement in the 444
 positive y -direction, U_y^N , for a value of $F = 0.01$ N is 445
 of magnitude 0.5276 mm. When we take the optimized 446
 material distribution obtained with $p = 3$ and run the 447
 forward analysis with $p = 1$, we obtain the value of 448
 U_y^N as 0.5157 mm. Therefore, the $p = 1$ design is 449
 similar to the $p = 3$ design in both material distribution 450
 and displacement performance. The result indicates that for 451
 this problem, penalization is not necessary to achieve a 452
 binary solution. This can be explained by the fact that the 453
 optimizer naturally seeks a design in which the transition 454
 temperatures of the two material regions are as far apart 455
 as possible in order to maximize the disparity in strain 456
 response at the end of stage III of the thermo-mechanical 457
 programming cycle. This will lead to the largest tip 458
 deflection. 459

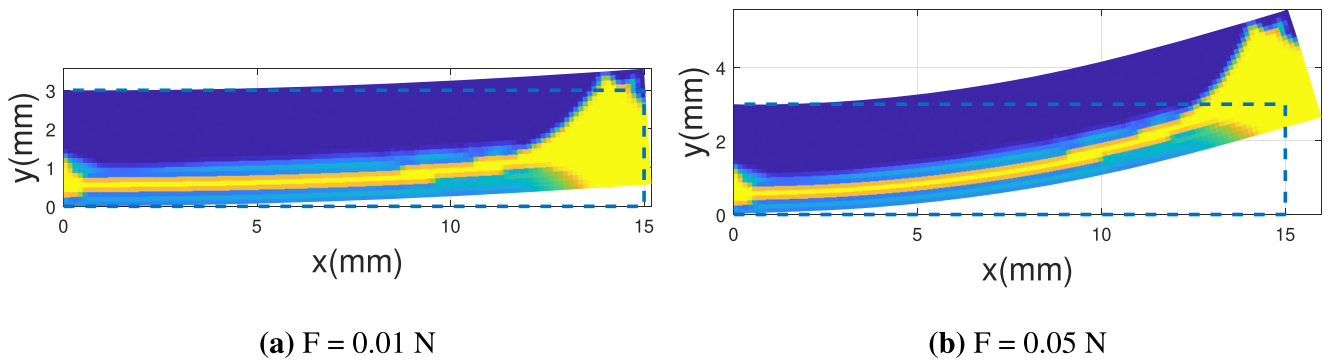


Fig. 8 Maximum bending deflection for different amounts of uniaxial stretching during the thermo-mechanical programming cycle

460 To compare the performances of the optimized structure
 461 under the influence of the reduced and full thermo-
 462 mechanical cycle, the optimized structure shown in Fig. 11
 463 was analyzed subject to the full thermo-mechanical cycle.
 464 To simulate comparable loading and cooling conditions,
 465 the optimized structure was subjected to a constant load of
 466 $F = 0.01\text{ N}$ at temperature T_H for a total time of 20 min
 467 simulated with 4 time steps. Then it was allowed to relax,
 468 while the external deformation was held constant, for a time
 469 of 10 min simulated with 2 time steps. Holding the external
 470 deformations constant, the temperature was decreased from
 471 T_H to T_L over a time of 20 min simulated with 4 time
 472 steps. Then, the structure was allowed to relax without any
 473 external constraints for a total time of 15 min simulated
 474 with 3 time steps. This was followed by increasing the
 475 temperature from T_L to T^* over a duration of 10 min.
 476 The tip deflection was found to be 0.5686 mm. The 7.7%

477 increase in the tip deflection can be attributed to the fact that
 478 the structure was subjected to loading at higher temperatures
 479 for longer duration due to which it stretched more during
 480 the deformation stage. This led to the slight increase in the
 481 final tip deflection measured at the end of the heating step.

482 Figure 12 shows the optimized self-actuating beam for
 483 different initial starting points with $p = 1$. Here, three
 484 additional starting points have been explored. Figure 12b
 485 shows the optimized material distribution for a random
 486 initialization of the design variable. The value of U_y^N is
 487 0.5301 mm in the positive y -direction. Figure 12d shows
 488 the optimized material distribution for an informed guess
 489 with the upper-half of the beam initialized to $\rho = 0$ and
 490 the lower-half of the beam initialized to $\rho = 1$. The value of
 491 U_y^N is 0.5303 mm in the positive y -direction for this case.
 492 Figure 12f shows the optimized material distribution for an
 493 uniform initial guess with $\rho = 1.0$. The final value of U_y^N

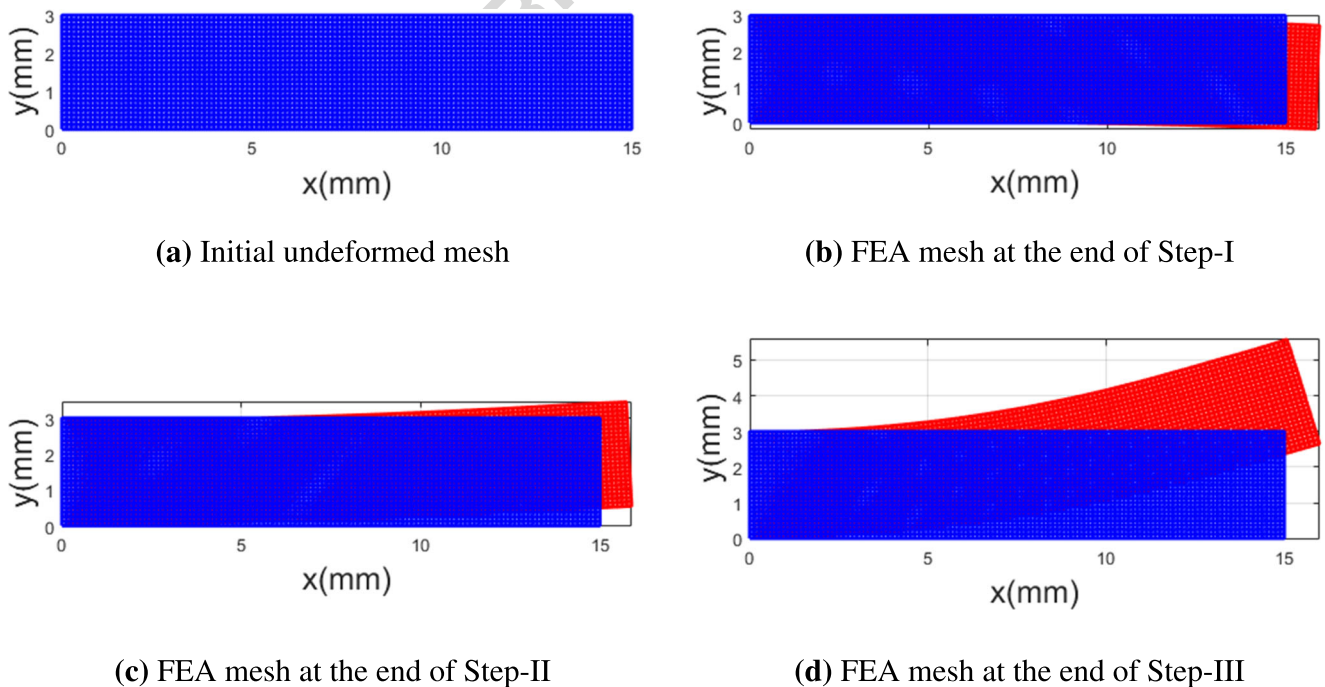


Fig. 9 Finite element meshes of the self-actuating beam at each stage of the condensed thermo-mechanical programming cycle for $F = 0.05\text{ N}$

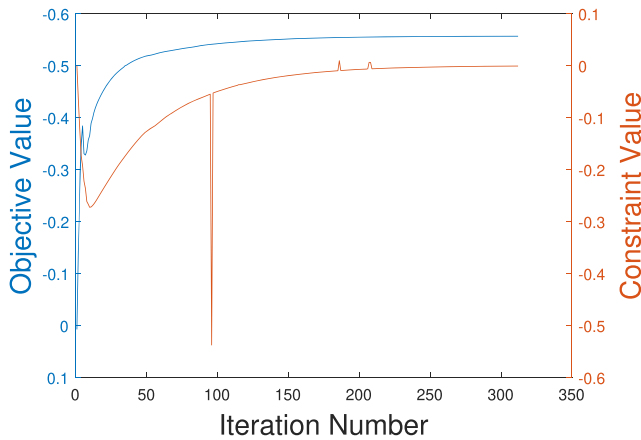


Fig. 10 Convergence history of the objective and constraint functions for the self-actuating beam optimization

494 is 0.5291 mm. We observe that in all of these cases, the
 495 material distribution converges to a pattern similar to that
 496 obtained using a *neutral* starting point in which all elements
 497 have the same initial material fraction. The results suggest
 498 that the conventional approach of using a *neutral* starting
 499 point yields satisfactory results.

500 **6.2 Self-actuating gripper (SAG) design**

501 The second case study discusses the design of an SMP-
 502 based self-actuating gripper. The loading and boundary
 503 conditions are shown in Fig. 13. The optimization problem
 504 statement is similar to that of the self-actuating beam
 505 design problem with the displacement U_y^N in the downward
 506 direction. Here, we have used the symmetry of the design
 507 domain to optimize the distribution of material only on the
 508 top-half. This reduces the computational cost by reducing
 509 the effective size of the mesh; as a result, only the
 510 displacement of a single node (marked with a red dot) is
 511 used for the optimization problem formulation. The design
 512 domain has dimensions 100 mm \times 100 mm and is meshed
 513 with 7200 equally sized 4-node square elements. The
 514 square-shaped cutout has dimensions of 25 mm \times 25 mm.
 515 The force (F) applied during step I is 0.017 N. The
 516 whole structure is subjected to the SMP-modified thermo-
 517 mechanical cycle, and the goal of the topology optimization
 518 algorithm is to maximize the displacement at the end of

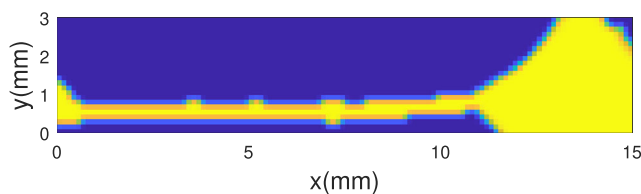


Fig. 11 Optimized material distribution with penalization parameter $\rho = 1$

step III. The idea behind maximizing the displacement is to
 519 achieve a gripping motion. 520

Figure 14 shows the optimized distribution of the two
 521 SMP materials inside the design domain with maximized
 522 tip displacement of the gripper. Figure 16 shows the
 523 deformed SAG configuration superimposed on the original
 524 undeformed shape shown by the red dashed lines. The
 525 optimized value of U_y^N obtained with a loading of 0.017
 526 N is 2.3472 mm, in the negative y -direction. As explained
 527 in Section 6.1, a higher quantity of the SMP^1 material,
 528 with lower glass-transition temperature, is concentrated near
 529 the node N , interspersed with the SMP^2 material, having
 530 the higher glass-transition temperature. As the temperature
 531 reached T^* , at the end of the step III, the SMP^1 material
 532 tries to contract due to the conversion of glass phase to
 533 rubber phase inside the material. This contraction is resisted
 534 by the finger-like regions, consisting of SMP^2 , which still
 535 has a predominant glass phase. This strain imbalance leads
 536 to the bending of the jaws, giving rise to the gripping action.
 537 The SAG design for a mesh size of 120 \times 60 took over
 538 215,136 core-hours on 144 processors and 498 optimization
 539 iterations to generate the above design. 540

The optimization convergence history of the objective
 541 and constraint functions for the design of the self-actuating
 542 gripper is shown in Fig. 17. 543

544 **6.3 Design of a 3D torsional structure**

To expand the current framework to design 3D structures,
 545 we have applied the above-described methodology to the
 546 design of a torsional unit structure. The unit structure
 547 will exhibit torsion about the axis along which the unit is
 548 stretched during the programming cycle. The design domain
 549 for the structure is shown in Fig. 18. It has dimensions of
 550 100 mm \times 20 mm \times 20 mm and is discretized with 25 \times 5 \times
 551 5, 8 node cubic elements. The design domain is fixed at
 552 one end while a force (F) of 0.05 N is applied during the
 553 thermo-mechanical programming cycle as shown in Fig. 18.
 554

The objective is to tailor the material distribution
 555 inside the design domain such that the displacement in z -
 556 direction at the degree-of-freedom, U_z^{2N} , is minimized at
 557 the end of the step III of the thermo-mechanical cycle,
 558 while constraining the U_z^1 d.o.f to be in the positive z -
 559 direction, greater than a certain baseline value U_0 , also
 560 evaluated at the end of step III. The total amount of SMP^1
 561 material used is also constrained to a maximum limit of
 562 $V_{SMP^1}^{max}$. Mathematically, the optimization problem can be
 563 formulated as: 564

$$\begin{aligned} & \text{minimize} \quad U_z^2|_{t=T^*} \\ & \quad \quad \quad \rho \\ & \text{subject to} \quad V_{SMP^1}(\rho) \leq V_{SMP^1}^{Max}, \quad 0 \leq \rho \leq 1 \\ & \quad \quad \quad U_z^1|_{t=T^*} > U_0 \end{aligned} \quad (29)$$

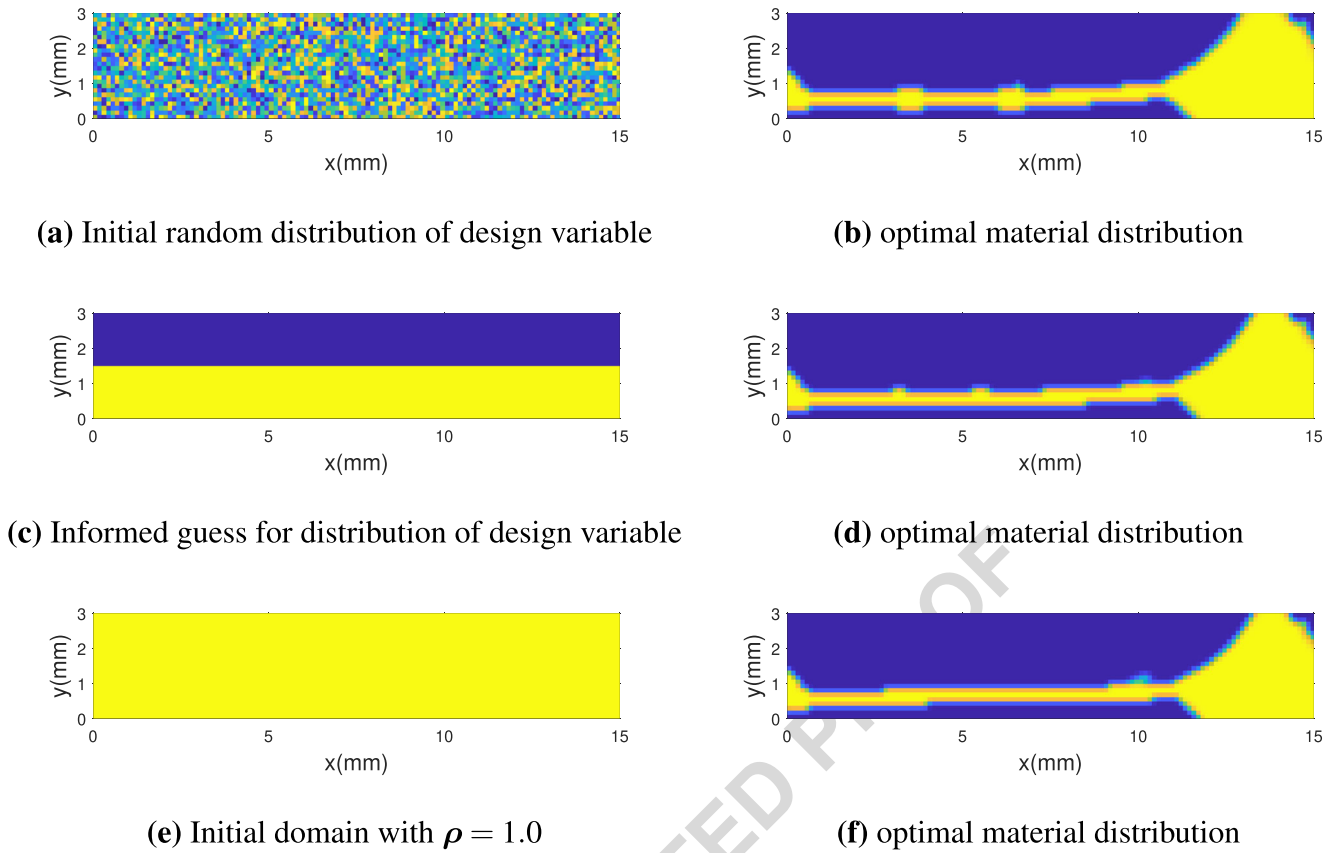


Fig. 12 Optimized material distribution for different initial conditions

The constant U_0 is evaluated as:

565

$$U_0 = 0.8(U_z^1)_{initial} \tag{30}$$

where $(U_z^1)_{initial}$ refers to the U_z^1 for the initial design domain corresponding to the application a uniaxial force before the start of the optimization. Figure 19 shows the optimized material distribution for the 3D torsional structure design problem. For a force of $F = 0.05 N$,

566
567
568
569
570

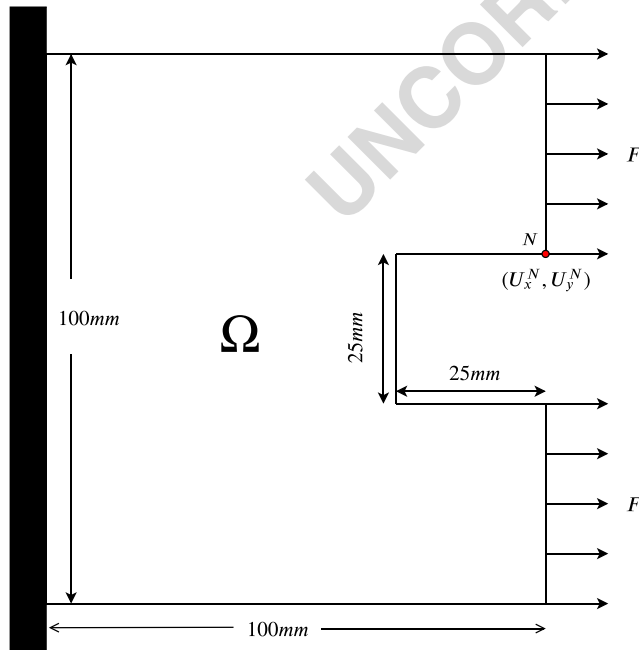


Fig. 13 Initial design domain of the self-actuating gripper with boundary conditions and loading conditions

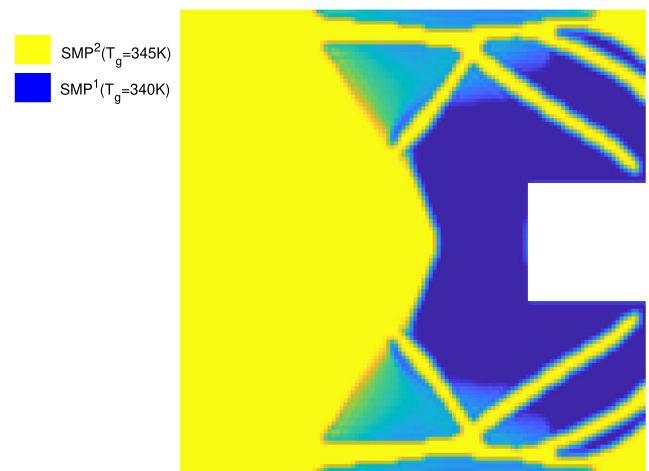


Fig. 14 Optimized material distribution for the self-actuating gripper design

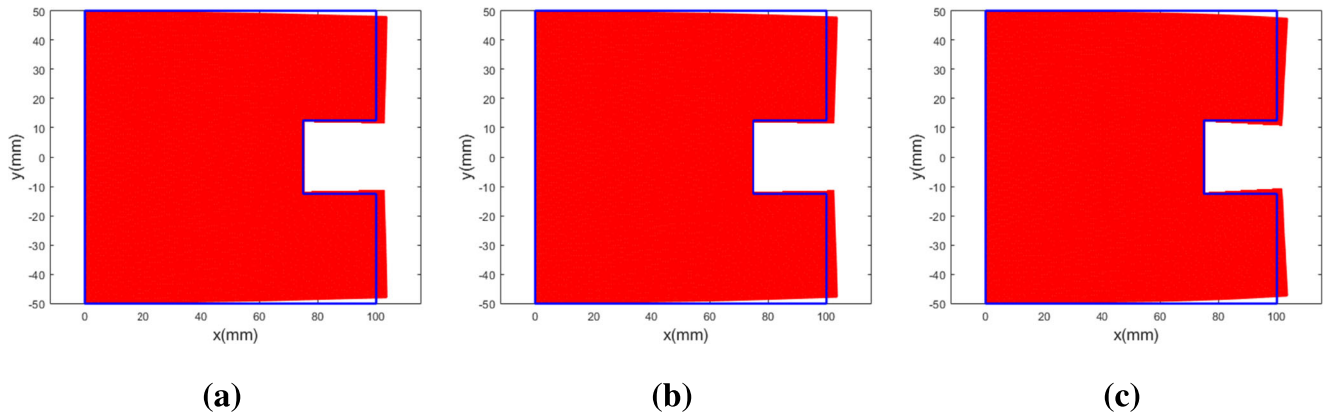


Fig. 15 Self-actuating gripper mesh at different stages of the condensed thermo-mechanical programming cycle. **a** Deformed mesh at the end of the step I. **b** Deformed mesh at the end of step II. **c** Mesh at the end of step III

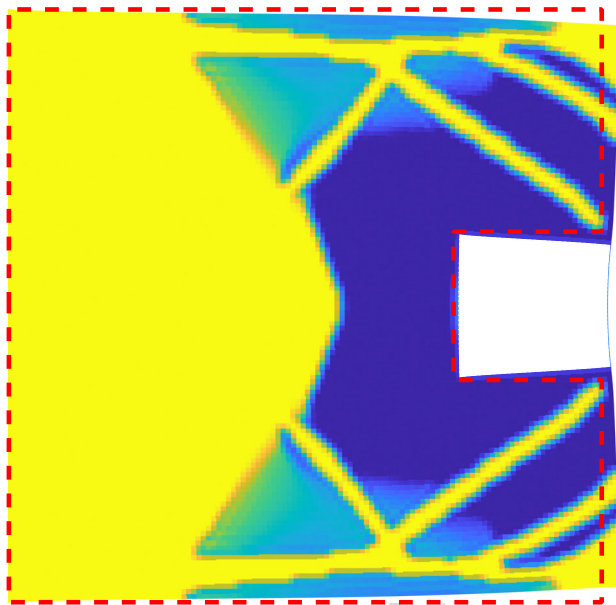


Fig. 16 Comparison of the SAG in the deformed configuration with the original undeformed domain (dashed red line)

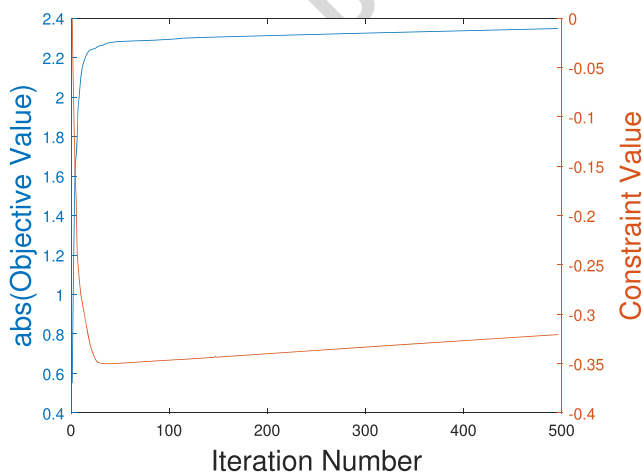


Fig. 17 Convergence history of the objective and constraint functions for the self-actuating gripper optimization

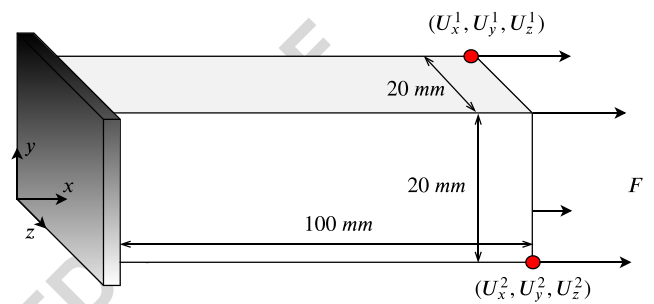


Fig. 18 Design domain and boundary conditions for the 3D torsional unit structure

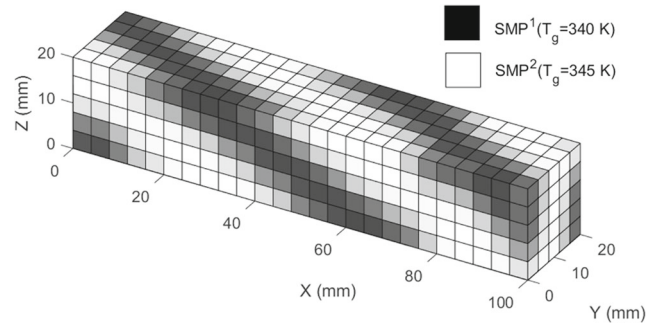


Fig. 19 Optimized material distribution for 3D torsional structure

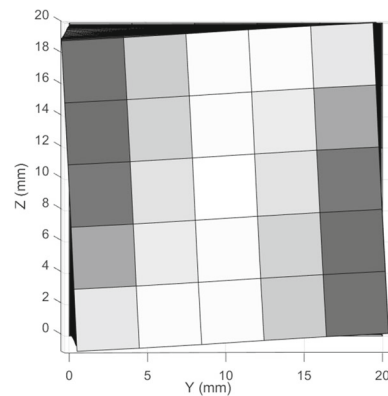


Fig. 20 The 3D torsional structure after deformation due to shape memory response (view from the free face at $x = 100$ mm)

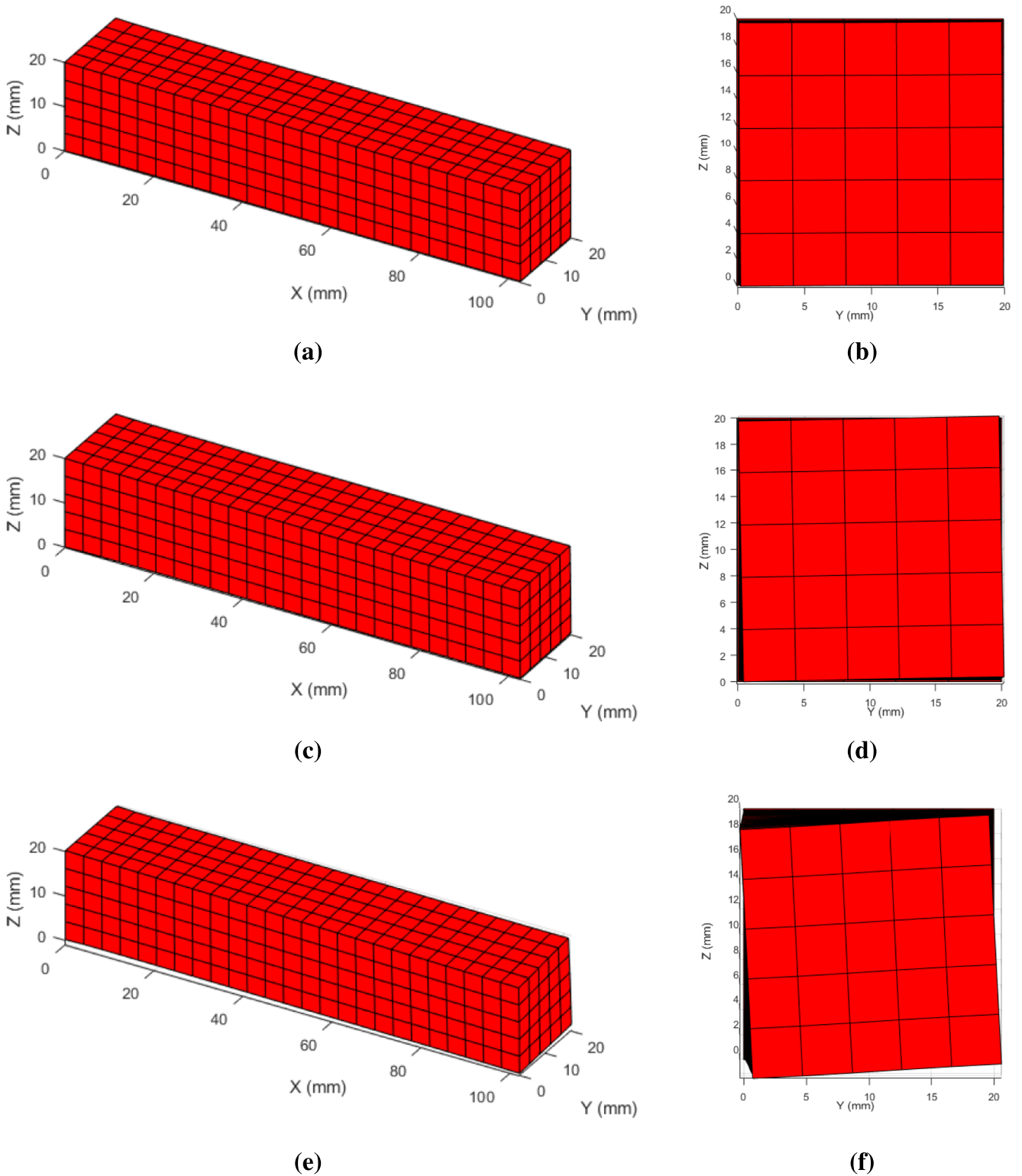


Fig. 21 3D optimized torsional structure at different stages of the modified thermo-mechanical cycle. **a, b** Isometric and front views of the deformed mesh at the end of step I. **c, d** Isometric and front views of

the deformed mesh at the end of step II. **e, f** Twisted mesh at the end of step III of the modified thermo-mechanical cycle

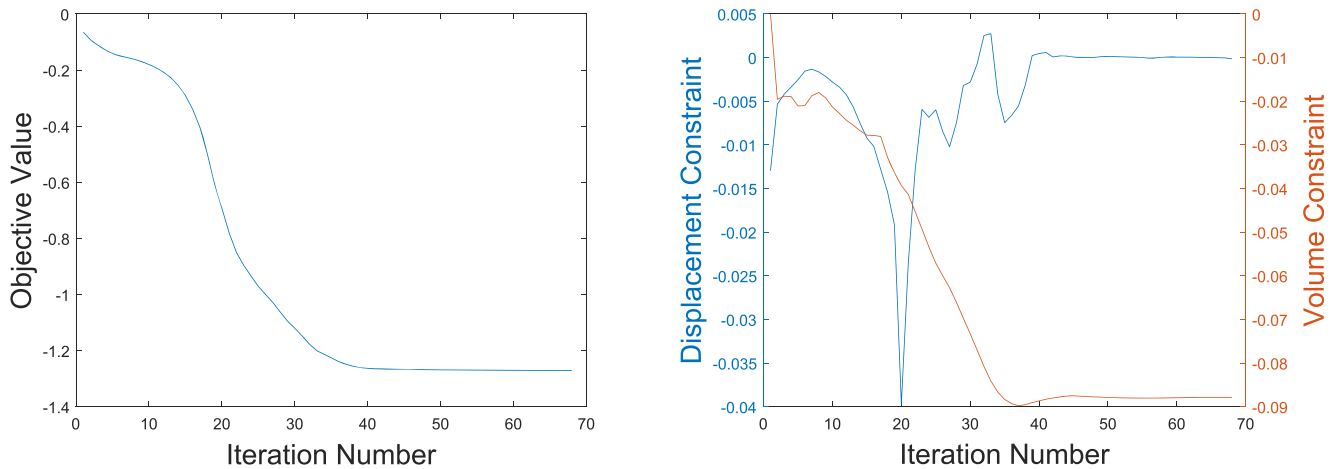


Fig. 22 Optimization convergence history for the 3D torsional structure optimization

571 the displacements of U_z^2 and U_z^1 are -1.2710 mm and
 572 0.5985 mm respectively.

573 We can observe from Fig. 19 that the SMP^1 and SMP^2
 574 materials are arranged as bands, running diagonally across
 575 the structure, very similar to the helical and spiral structural
 576 arrangements found in natural twisted structures.

577 Figure 20 shows twisting of the structure achieved
 578 through optimal distribution of SMP materials with
 579 simple axial stretching of the structure applied during the
 580 programming cycle.

581 The deformation of the structural mesh at different stages
 582 of the modified thermo-mechanical cycle of the 3D torsional
 583 structure for the optimized material layout is shown in
 584 Fig. 21. The convergence history of the objective function
 585 and the constraints for the design of the 3D torsional
 586 structure is shown in Fig. 22.

587 Figure 23 shows the optimized design domain with the
 588 penalization constant $p = 1$. For a force of $F = 0.05$ N,
 589 the displacements of U_z^2 and U_z^1 are -1.2024 mm and

0.4868 mm respectively. When we take the final optimized
 material distribution for $p = 3$ and run the forward analysis
 with $p = 1$, we obtain the value of the displacements
 U_z^2 and U_z^1 as -1.1956 mm and 0.0554 mm respectively.
 We observe that the absolute value of U_z^2 increases from
 1.1956 mm for $p = 3$ to 1.2024 mm for $p = 1$.

7 Conclusion

A novel framework for computationally designing multima-
 terial active structures containing SMPs was implemented
 to optimally exploit the material's shape memory charac-
 teristics. The constitutive modelling of SMPs proposed by
 Baghani et al. (2012) was implemented on a finite-element
 framework using the PETSc library to simulate SMP behav-
 ior over the thermo-mechanical cycle. The structural defor-
 mations and the thermally activated shape memory response
 were analyzed using a small-strain, multi-phase FEA model.
 The gradient information required for topology optimization
 was calculated using a time-dependent adjoint sensitivity
 analysis. A recursive algorithm for sensitivity analysis,
 necessary for accurately capturing the path-dependent char-
 acteristics of the SMPs, was introduced and the details
 of its implementation have been provided. A novel con-
 densed SMP thermo-mechanical programming cycle has
 been proposed to significantly reduce the computational
 cost involved in the analysis of the SMPs, while pre-
 serving the essential SMP characteristics. A fully parallel
 PETSc-based framework for topology optimization with
 multiple SMP materials was developed and implemented
 to well-refined multi-functional, multimaterial SMP struc-
 tures. Three numerical results showcasing the application

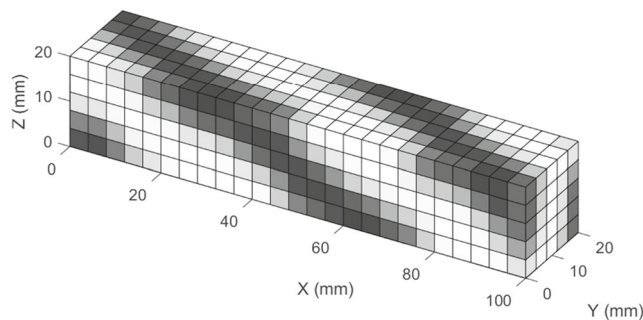


Fig. 23 Optimized material distribution for 3D torsional structure with $p = 1$

620 of the current framework have been provided. Topology
 621 optimization was implemented to design a morphing beam
 622 capable of deforming in a non-axial direction with simple
 623 axial loading applied during the thermo-mechanical pro-
 624 gramming cycle. Design of a self-actuating gripper was also
 625 implemented. To further expand the scope of the current
 626 framework, a 3D torsional structure was designed capable of
 627 twisting about the axis along which it is stretched during the
 628 thermo-mechanical programming cycle. The results show
 629 that topology optimization can be successfully implemented
 630 to tailor the distribution of SMP materials in the unde-
 631 formed domain so that when actuated using an external ther-
 632 mal stimulus, the structures exhibit different morphologies
 633 while fulfilling the required objectives. This research con-
 634 tributes to bridging the gap between computational design,
 635 and 4D printing. Future work will focus on design and 4D
 636 printing of multimaterial mechanisms with complex motion,
 637 including large deformations.

638 **Funding** The authors received financial support of the National
 639 Science Foundation under grant # CMMI-1663566.

640 **Compliance with ethical standards**

641 **Conflict of interest** The authors declare that they have no conflict of
 642 interest.

643 **Replication of results** Detailed descriptions of the algorithms used to
 644 generate all results are provided throughout the paper. Additionally,
 645 we have included all relevant material properties, and all algorithm
 646 parameters. Copies of the code used to generate the results will be
 647 made available upon request.

648 **Appendix 1: Finite element derivations**

649 The subscript, n , represents the time step.
 650 The terms \mathbb{A}_r , \mathbb{A}_g , \mathbb{H}_r , \mathbb{H}_g , \mathbb{B}_r , \mathbb{B}_g , and $\Delta\phi_{n+1}^g$ required
 651 in (A.2) are computed as:

$$\begin{aligned} \mathbb{A}_r &= (\mathbb{K}_{neq}^r + \mathbb{K}_{eq}^r) - \frac{\Delta t}{\eta_r} \mathbb{K}_{neq}^r \mathbb{H}_r^{-1} \mathbb{K}_{neq}^r \\ \mathbb{A}_g &= (\mathbb{K}_{neq}^g + \mathbb{K}_{eq}^g) - \frac{\Delta t}{\eta_g} \mathbb{K}_{neq}^g \mathbb{H}_g^{-1} \mathbb{K}_{neq}^g \\ \mathbb{H}_r &= \mathbb{I} + \frac{\Delta t}{\eta_r} \mathbb{K}_{neq}^r \\ \mathbb{H}_g &= \mathbb{I} + \frac{\Delta t}{\eta_g} \mathbb{K}_{neq}^g \\ \mathbb{B}_r &= \mathbb{H}_r^{-1} \mathbb{K}_{neq}^r \\ \mathbb{B}_g &= \mathbb{H}_g^{-1} \mathbb{K}_{neq}^g \\ \Delta\phi_{n+1}^g &= \phi_{n+1}^g - \phi_n^g \end{aligned} \tag{A.1}$$

The terms \mathbb{W}_r , \mathbb{W}_g , \mathbb{M} , \mathbb{N} , \mathbb{P} , \mathbb{O} , \mathbb{E} , and \mathbb{F} for (9) are defined 652
 as: 653

$$\begin{aligned} \mathbb{W}_r &= \mathbb{H}_r^{-1} \begin{bmatrix} \frac{\Delta t}{\eta_r} \mathbb{K}_{neq}^r \\ \eta_r \end{bmatrix} \\ \mathbb{W}_g &= \mathbb{H}_g^{-1} \begin{bmatrix} \frac{\Delta t}{\eta_g} \mathbb{K}_{neq}^g \\ \eta_g \end{bmatrix} \\ \mathbb{M} &= \frac{\Delta t}{\eta_i} \mathbb{A}_r \\ \mathbb{N} &= \frac{\Delta t}{\eta_i} \mathbb{B}_r \\ \mathbb{P} &= \Delta\phi_{n+1}^g \\ \mathbb{O} &= \mathbb{A}_g^{-1} \mathbb{A}_r \\ \mathbb{E} &= -\mathbb{A}_g^{-1} \mathbb{B}_r \\ \mathbb{F} &= v \mathbb{A}_g^{-1} \mathbb{B}_g \end{aligned} \tag{A.2}$$

Here, \mathbb{I} is the fourth-order identity tensor given by: 654

$$\begin{aligned} \mathbb{I}_{ijkl} &= \delta_{ik} \delta_{jl} \\ \delta_{ij} &= \begin{cases} 1, & \text{if } i = j, \\ 0, & \text{if } i \neq j. \end{cases} \end{aligned} \tag{A.3}$$

Here, δ_{ij} is the Kronecker delta. Isotropic linear elastic 655
 constitutive law is utilized to compute the fourth-order 656
 elasticity tensors \mathbb{K}_{eq}^r and \mathbb{K}_{neq}^r corresponding to the 657
 rubbery-phase and \mathbb{K}_{eq}^g and \mathbb{K}_{neq}^g for the glassy-phase 658
 material. 659

660 **Appendix 2: Derivation of sensitivity analysis**

Having discussed the generalized formulation for time- 661
 dependent adjoint sensitivity analysis in Section 5, we 662
 focus on deriving the sensitivity formulation specifically 663
 for shape memory polymers. To avoid confusion in the 664
 notation representing inelastic strain components and time 665
 steps, from here on the current time step will be denoted by 666
 subscript $\{n + 1\}$, the previous time step will be denoted by 667
 subscript $\{n\}$, and so on. 668

The sensitivity of the objective function is calculated 669
 via (25). This equation has two components: the first is 670
 the *adjoint* vectors (λ) and the other is the component 671
 capturing the explicit dependence of the residual term on the 672
 design variable. The *adjoint* vectors are computed via (24). 673
 Evaluation of both of these components requires the residual 674

675 term (\mathbf{R}). The residual equation for the SMP can be stated
 676 as:

$$\begin{aligned} \mathbf{R}_{n+1} = & \int_{\Omega} \mathbf{B}^T \mathbb{A}^{(r)} \mathbb{D}_{n+1}^{-1} : \mathbf{B} \mathbf{u}_{n+1} dv - \int_{\Omega} \mathbf{B}^T \mathbb{X}_{n+1}^{(r)} : \boldsymbol{\varepsilon}_n^{(ir)} dv \\ & + \int_{\Omega} \mathbf{B}^T \mathbb{X}_{n+1}^{(g)} : \boldsymbol{\varepsilon}_n^{(ig)} dv + \int_{\Omega} \mathbf{B}^T \mathbb{Y}_{n+1}^{(r)} : \boldsymbol{\varepsilon}_n^{(ir)} dv \\ & - \int_{\Omega} \mathbf{B}^T \mathbb{V}_{n+1} : \boldsymbol{\varepsilon}_n^{(i)} dv - \int_{\Omega} \mathbf{B}^T \mathbb{Z}_{n+1}^{(r)} : \boldsymbol{\varepsilon}_n^{(is)} dv \\ & - \int_{\Omega} \mathbf{B}^T \mathbb{A}^{(r)} \mathbb{D}_{n+1}^{-1} : \boldsymbol{\varepsilon}_{n+1}^{Th} dv - \mathbf{F}^{ext} \end{aligned} \quad (\text{B.1})$$

677 where the terms $\mathbb{X}_{n+1}^{(r)}$, $\mathbb{X}_{n+1}^{(g)}$, $\mathbb{Y}_{n+1}^{(r)}$, $\mathbb{V}_{n+1}^{(r)}$, $\mathbb{Z}_{n+1}^{(r)}$ are
 678 given by:
 679

$$\begin{aligned} \mathbb{X}_{n+1}^{(r)} &= \mathbb{A}_r \mathbb{D}_{n+1}^{-1} \phi_{n+1}^{(g)} \mathbb{A}_g^{-1} \mathbb{B}_r \\ \mathbb{X}_{n+1}^{(g)} &= \mathbb{A}_r \mathbb{D}_{n+1}^{-1} \phi_{n+1}^{(g)} \mathbb{A}_g^{-1} \mathbb{B}_g \\ \mathbb{Y}_{n+1}^{(r)} &= \mathbb{A}_r \mathbb{D}_{n+1}^{-1} \left(\frac{\Delta t}{\eta_i} \right) \mathbb{B}_r \\ \mathbb{V}_{n+1}^{(r)} &= \mathbb{A}_r \mathbb{D}_{n+1}^{-1} \\ \mathbb{Z}_{n+1}^{(r)} &= \mathbb{A}_r \mathbb{D}_{n+1}^{-1} \end{aligned} \quad (\text{B.2})$$

680 The differentiation of the residual equation, \mathbf{R}_{n+1} , with
 681 respect to the design variables can be computed by:

$$\begin{aligned} \frac{\partial \mathbf{R}_{n+1}}{\partial \boldsymbol{\rho}} &= \int_{\Omega} \mathbf{B} \frac{\partial \boldsymbol{\sigma}_{n+1}}{\partial \boldsymbol{\rho}} dv - \frac{\partial \mathbf{F}_{n+1}^{ext}}{\partial \boldsymbol{\rho}} \\ \frac{\partial \boldsymbol{\sigma}_{n+1}}{\partial \boldsymbol{\rho}} &= \frac{\partial \mathbb{A}_r}{\partial \boldsymbol{\rho}} : \boldsymbol{\varepsilon}_{n+1}^{(r)} + \mathbb{A}_r : \frac{\partial \boldsymbol{\varepsilon}_{n+1}^{(r)}}{\partial \boldsymbol{\rho}} - \frac{\partial \mathbb{B}_r}{\partial \boldsymbol{\rho}} : \boldsymbol{\varepsilon}_n^{(ir)} - \mathbb{B}_r : \frac{\partial \boldsymbol{\varepsilon}_n^{(ir)}}{\partial \boldsymbol{\rho}} \end{aligned} \quad (\text{B.3})$$

682 To evaluate the *adjoint* vectors, it is required to capture
 683 the explicit dependence of the residual for the k^{th} time step
 684 on the displacement of the i^{th} time step, i.e., $\frac{\partial \mathbf{R}_k}{\partial \mathbf{u}_i}$. These
 685 terms are referred to as the ‘‘coupling’’ terms. Finding the
 686 $\frac{\partial \mathbf{R}_k}{\partial \mathbf{u}_i}$ terms are more involved since at each time step there is
 687 an exponential growth of terms from the previous time step.

For example, let us evaluate the term $\frac{\partial \mathbf{R}_{n+1}}{\partial \mathbf{u}_{n-1}}$. The coupling
 term $\frac{\partial \mathbf{R}_{n+1}}{\partial \mathbf{u}_{n-1}}$ is proportional to $\frac{\partial \mathbf{R}_{n+1}}{\partial \boldsymbol{\varepsilon}_{n-1}^{(r)}}$, since strain is a linear
 function of displacement (u). We can use the chain rule to
 write:

$$\frac{\partial \mathbf{R}_{n+1}}{\partial \mathbf{u}_{n-1}} \propto \frac{\partial \mathbf{R}_{n+1}}{\partial \boldsymbol{\varepsilon}_{n-1}^{(r)}} \approx \underbrace{\frac{\partial \mathbf{R}_{n+1}}{\partial \boldsymbol{\varepsilon}_{n-1}^{(r)}}}_{\text{term I}} \underbrace{\frac{\partial \boldsymbol{\varepsilon}_{n-1}^{(r)}}{\partial \boldsymbol{\varepsilon}_{n-1}}}_{\text{term II}} \quad (\text{B.4})$$

Equation (B.4) gets contributions from *term I* and *term II*.
 The parameter \mathbf{R}_{n+1} which represents the residual, obtained
 during the forward analysis, is given by (B.1) which has
 seven terms. Each of the terms, at a particular time step, is
 dependent not only on the current time step of the evaluation
 but also on the previous time step as shown in (9). For
 example, if we calculate the coupling coefficients from the
 second term, $\int_{\Omega} \mathbf{B}^T \mathbb{X}_{n+1}^{(r)} \boldsymbol{\varepsilon}_n^{(ir)} dv$, of the residual equation,
 and track the evolution of the term in time, we will get the
 map as shown in Fig. 24. The coefficient C_f is defined as:

$$C_f = \mathbf{B}^T \mathbb{X}_{n+1}^{(r)}$$

The terms \mathbb{A}_n and \mathbb{B}_n are given by:

$$\begin{aligned} \mathbb{A}_n &= \mathbb{D}_n^{-1} \left[-\phi_n^g \mathbb{A}_g^{-1} \mathbb{B}_r + \frac{\Delta t}{\eta_i} \mathbb{B}_r \right] \\ \mathbb{B}_n &= \mathbb{D}_n^{-1} \left[\phi_n^g \mathbb{A}_g^{-1} \mathbb{B}_g \right] \end{aligned}$$

If we collect the terms to evaluate $\frac{\partial \boldsymbol{\varepsilon}_n^{(ir)}}{\partial \boldsymbol{\varepsilon}_{n-1}^{(r)}}$, we get:

$$\begin{aligned} \frac{\partial \boldsymbol{\varepsilon}_n^{(ir)}}{\partial \boldsymbol{\varepsilon}_{n-1}^{(r)}} &= \left[\mathbb{H}_r^{-1} \mathbb{W}_r + \mathbb{W}_r \mathbb{A}_n \mathbb{W}_r + \mathbb{W}_r \mathbb{B}_n \mathbb{W}_g \circ \right. \\ &\quad \left. + \mathbb{W}_r \mathbb{D}_n^{-1} \mathbb{M} + \mathbb{W}_r \mathbb{D}_n^{-1} \mathbb{P} \right] \end{aligned} \quad (\text{B.5})$$

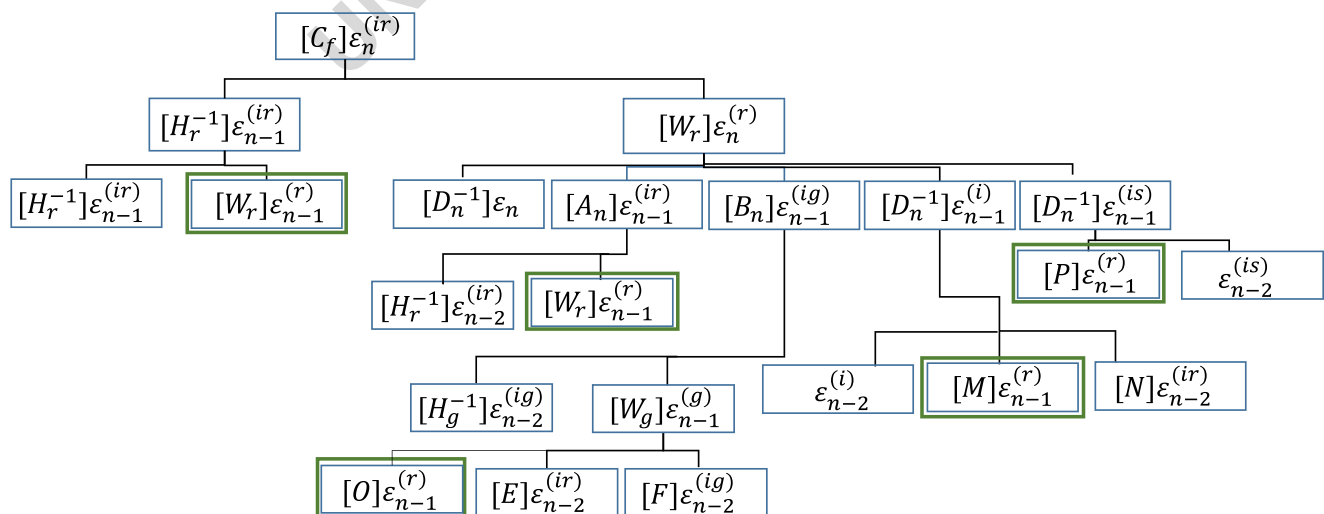


Fig. 24 Tracking $\frac{\partial \boldsymbol{\varepsilon}_n^{(ir)}}{\partial \boldsymbol{\varepsilon}_{n-1}^{(r)}}$ terms in time

704 Equation (B.5) represents *term I* in terms of $\varepsilon_n^{(ir)}$. A similar
 705 procedure is adopted for all the other six terms present in the
 706 (B.1) to make a total of twenty-three terms for the coupling
 707 term $\frac{\partial R_{n+1}}{\partial u_{n-1}}$. The computation of *term II* is straightforward
 708 and is given by:

$$\frac{\partial \varepsilon_{n-1}^{(r)}}{\partial \varepsilon_{n-1}} = \mathbb{D}_{n-1}^{-1} \tag{B.6}$$

709 Capturing the evolution of all the components required to
 710 accurately calculate the sensitivities makes this process compu-
 711 tationally expensive and a highly time-consuming procedure.
 712 The time taken increases exponentially with the total number
 713 of time steps required to simulate the thermo-mechanical
 714 cycle of the SMP increases. The function and the recursive
 715 algorithm used to compute the $\{\frac{\partial R_k}{\partial u_i}\}$ terms for the total
 716 sensitivity analysis are shown in Algorithms 2 and 3. Note
 717 that for the recursive algorithm shown in Algorithm 3,
 718 parameters k and i represent the time steps. Here, the func-
 719 tions `func_eir`, `func_eig`, `func_is`, and `func_i`
 720 are programmable versions of $\mathbf{e}^{(ir)}$, $\mathbf{e}^{(ig)}$, $\mathbf{e}^{(is)}$, and $\mathbf{e}^{(i)}$,
 721 shown in (9), implemented for the k^{th} step. The variable
 722 $[M]$ is a collection of parameters representing the intrinsic
 723 material properties. The function f represents a general
 724 function manipulating its inputs and giving a desired output.

Algorithm 2 Psuedocode to calculate the terms $\frac{\partial R_k}{\partial u_i}$ for the sensitivity evaluation.

```

sens_partI(k, i, M)
Cf = f(M) /* compute external variable
Cf as a function of M */
/* call individual recursive
functions */
 $\frac{\partial \varepsilon_k^{(ir)}}{\partial \varepsilon_i^{(r)}} \leftarrow \text{func\_eir}(C_f, k, i, M)$ 
 $\frac{\partial \varepsilon_k^{(ig)}}{\partial \varepsilon_i^{(r)}} \leftarrow \text{func\_eig}(C_f, k, i, M)$ 
 $\frac{\partial \varepsilon_k^{(is)}}{\partial \varepsilon_i^{(r)}} \leftarrow \text{func\_is}(C_f, k, i, M)$ 
 $\frac{\partial \varepsilon_k^{(i)}}{\partial \varepsilon_i^{(r)}} \leftarrow \text{func\_i}(C_f, k, i, M);$ 
term I =  $f\left(\frac{\partial \varepsilon_k^{(ir)}}{\partial \varepsilon_i^{(r)}}, \frac{\partial \varepsilon_k^{(ig)}}{\partial \varepsilon_i^{(r)}}, \frac{\partial \varepsilon_k^{(is)}}{\partial \varepsilon_i^{(r)}}, \frac{\partial \varepsilon_k^{(i)}}{\partial \varepsilon_i^{(r)}}\right)$  /* term
I of (B.4) is calculated using the
output of the individual recursive
functions */
term II =  $f\left(\frac{\partial \varepsilon_i^{(r)}}{\partial \varepsilon_i}\right)$  /* term II of
(B.4) is calculated */
Return:  $\frac{\partial R_k}{\partial u_i} \leftarrow f(\text{term I}, \text{term II})$ 
    
```

726 The individual functions have similar structures and one
 727 such function `func_eir` has been shown in details in
 728 Algorithm 3.
 729

Algorithm 3 Recursive algorithm to capture strain evolution with time for the sensitivity evaluation.

```

func_eir(Cf, k, i, M)
CI =  $\mathbb{H}_r^{-1}$  /* compute internal
variable CI */
 $\frac{\partial \varepsilon_k^{(r)}}{\partial \varepsilon_i^{(r)}} \leftarrow \text{func\_er}(CI, k, i, M)$  /* call
function which tracks evolution of
strain variables as shown in (B.5) */
if  $k > i$  then
 $\frac{\partial \varepsilon_{k-1}^{(ir)}}{\partial \varepsilon_i^{(r)}} \leftarrow \text{func\_eir}(C_f \times CI, k-1, i, M)$ 
/* call itself with  $k = k-1$  */
Return:  $\frac{\partial \varepsilon_k^{(r)}}{\partial \varepsilon_i^{(r)}} + \frac{\partial \varepsilon_{k-1}^{(ir)}}{\partial \varepsilon_i^{(r)}}$  /* output */
    
```

To verify the implementation of the sensitivity analysis,
 the design domain shown in Fig. 5 is discretized with a
 coarse mesh of 45 elements. The structure is initialized
 with a uniform distribution of design variable $\rho = 0.3$.
 It was then subjected to an axial stretching load $\mathbf{F} =$
 $0.025 N$ during the cooling phase of the thermo-mechanical
 cycle. The load was removed during the relaxation and
 heating phases of the thermo-mechanical programming
 cycle. The function of interest is the tip displacement \mathbf{u}_a^M
 as shown in (19). In this case, the parameter a is the y -
 degree-of-freedom of the node shown in Fig. 5 and M is
 the time step at the end of the step III of the thermo-
 mechanical programming cycle. The material parameters
 used for this analysis are same as listed in Table 1. The
 adjoint method and the forward difference method were
 used to evaluate the derivative of the tip displacement with
 respect to the mixing ratio of each element. Figure 25 shows

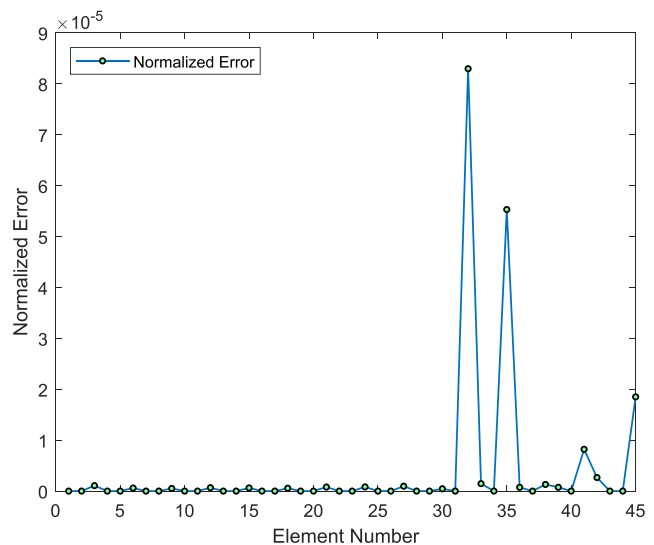


Fig. 25 Comparison between the sensitivity values evaluated through the finite-difference scheme and the adjoint formulation

Table 2 Sensitivity values evaluated through the adjoint formulation and the finite difference method

Element no.	Adjoint sensitivities	Finite difference sensitivities	Normalized error ($\times 10^{-6}$)
1	-0.2416477	-0.2416476	0.482
2	-0.0000000	-0.0000001	-
3	0.2416477	0.2416475	1.07
4	-0.2543351	-0.2543351	0.00
5	0.0000000	0.0000000	0.00
6	0.2543351	0.2543350	0.599
7	-0.2375154	-0.2375154	0.00
8	0.0000000	0.0000000	0.00
9	0.2375154	0.2375153	0.516
10	-0.2225283	-0.2225282	0.376
11	0.0000000	0.0000000	0.00
12	0.2225283	0.2225281	0.661
13	-0.2038087	-0.2038086	0.359
14	0.0000000	0.0000000	0.00
15	0.2038086	0.2038085	0.619
16	-0.1844918	-0.1844917	0.539
17	-0.0000001	-0.0000001	0.00
18	0.1844916	0.1844915	0.563
19	-0.1650572	-0.1650571	0.244
20	-0.0000010	-0.0000010	0.00
21	0.1650567	0.1650565	0.793
22	-0.1456293	-0.1456293	0.00
23	-0.0000042	-0.0000041	-
24	0.1456292	0.1456291	0.818
25	-0.1262059	-0.1262059	0.00
26	-0.0000104	-0.0000104	0.00
27	0.1262118	0.1262119	0.958
28	-0.1067716	-0.1067717	0.454
29	-0.0000017	-0.0000017	0.00
30	0.1068102	0.1068101	0.441
31	-0.0873091	-0.0873091	0.00
32	0.0001378	0.0001379	82.9
33	0.0874321	0.0874320	1.46
34	-0.0678103	-0.0678104	0.276
35	0.0008085	0.0008084	55.2
36	0.0680543	0.0680542	0.724
37	-0.0488513	-0.0488514	1.12
38	0.0027865	0.0027864	1.30
39	0.0480513	0.0480513	0.00
40	-0.0302951	-0.0302951	0.00
41	0.0042528	0.0042528	0.00
42	0.0250887	0.0250886	2.65
43	-0.0388250	-0.0388251	0.415
44	-0.0123738	-0.0123738	0.00
45	0.0027180	0.0027181	18.5

749 the normalized error of the sensitivity values obtained by
 750 the finite-difference approach and the adjoint sensitivity
 751 analysis. The normalized error (NE) for each element is
 752 evaluated as:

$$NE = \left| \frac{adjoint - FD}{FD} \right| \quad (B.7)$$

753 Note that for elements where the sensitivity is at or near
 754 zero, we have omitted the normalized error to avoid the
 755 indication of an artificially high error due to an extremely
 756 small denominator. The displacement obtained at the end of
 757 step III was -0.0130 mm. The sensitivity values obtained
 758 through the adjoint formulation and the finite-difference
 759 method are tabulated in Table 2. The maximum error
 760 between these values was found to be 2.6×10^{-7} . This
 761 established that the framework developed can successfully
 762 compute the sensitivities for SMP materials with a high
 763 degree of accuracy.

764 Figure 26 shows the time required to calculate $\frac{\partial R_{n+1}}{\partial u_{n-7}}$,
 765 the contribution of a total of 8 simulation steps, for a
 766 finite-element mesh of 50 elements by a single processor.
 767 As we can see, just using eight steps to simulate the
 768 entire SMP thermo-mechanical programming cycle even for
 769 a coarse mesh can incur high computational costs. This
 770 result motivated the development of PETSc-based parallel
 771 implementation of the FEA and sensitivity evaluation
 772 framework using CPUs on the *Golub Cluster* at the
 773 University of Illinois. Since the bottleneck for the entire
 774 algorithm is the sensitivity evaluation and particularly
 775 the time-dependent algorithm, the parallelization is done
 776 with the objective of distributing the elements onto the

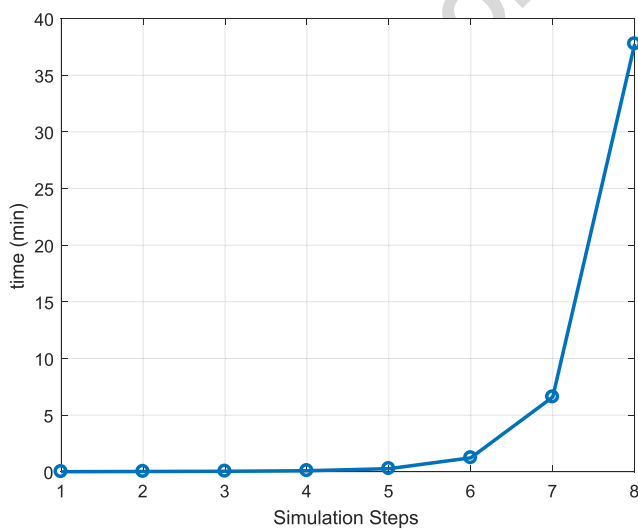


Fig. 26 Computation time required for tracking $\frac{\partial \epsilon_n^{ir}}{\partial \epsilon_{n-1}^r}$ terms

processors such that each processor has the optimum
 number of elements for efficient computations. A total
 of 144 processors (6 nodes with 24 processors each)
 were utilized for generating the 2D results. For the 3D
 optimization implementation, a total of 250 processors
 (10 nodes with 25 processors each) were utilized. The
 structural optimization problem is solved using the Method
 of Moving Asymptotes (MMA) (Svanberg 1987). The
 PETSc implementation of the MMA algorithm is based on
 the paper by Aage et al. (2015).

Appendix 3: Validation of the finite element model

After implementing the constitutive model using the finite
 element framework for a single shape memory polymer
 material with the material properties as tabulated in Table 1
 for SMP^1 , the accuracy of the implementation was verified
 against existing experimental and computational results
 from the literature. The results and the comparisons here
 are for the *full* thermomechanical programming cycle, not
 the modified cycle described in Fig. 3. Two broad cases,
 time-independent SMP behavior and time-dependent SMP
 behavior, were analyzed and their results were compared.

3.1 Time-independent SMP behavior

To verify the current finite element implementation, the
 results obtained for a time-independent *stress free strain*
recovery cycle were compared with the experimental results
 obtained by Liu et al. (2006). Figure 27b shows that the
 internal stress in a SMP sample increases as the temperature
 is reduced. This increase in the internal stress is due to
 an increase in the thermal stresses since the sample cannot
 contract with the decrease of temperature. We can observe
 that near the vicinity of the glass-transition temperature,
 the internal stress is negligible. This can be attributed to
 the low thermal stresses in this region. In the regions
 away from the glass-transition temperature, the internal
 stress increases sharply due to the presence of the glassy
 phase. The nature of evolution of the internal stresses, as
 observed experimentally in Fig. 27a for different amounts
 of pre-strains, is captured successfully by the current
 implementation. The discrepancies in the magnitude of the
 stresses can be attributed to the different materials used
 in the experimental studies and the numerical simulations.
 The difference in the material properties arises mainly
 due to the fact that the current analysis is geared toward
 application in the topology optimization algorithm and is

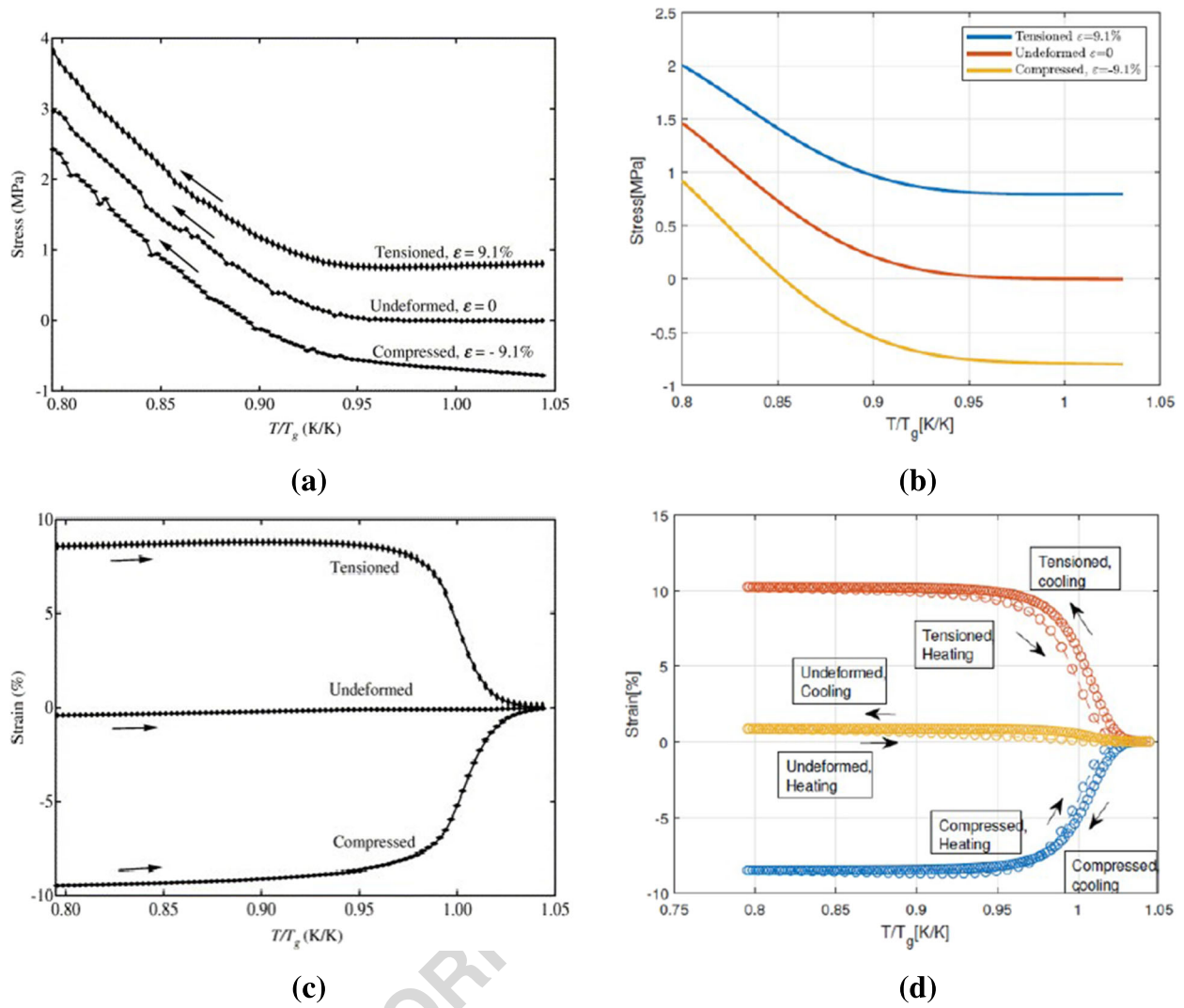


Fig. 27 a, c Experiments reported by Liu et al. (2006) for the stress free strain recovery cycle. b, d Results from the current FEM implementation

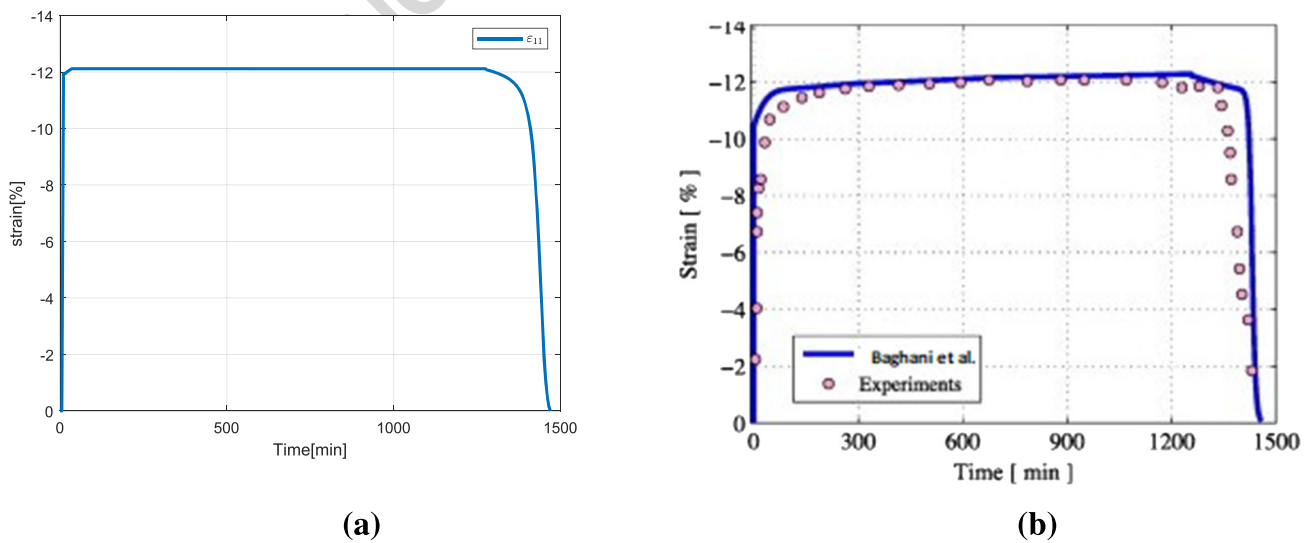


Fig. 28 a Reproduction of the shape memory effect (stress free strain recovery) as captured by the current implementation. b Numerical implementation done by Baghani et al. (2012) for experiments reported by Li and Nettles (2010)

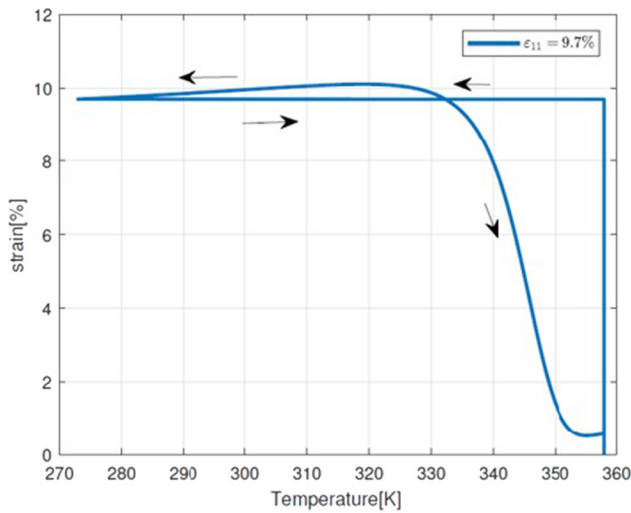
822 based on the rheological model as shown in Fig. 2, where
 823 the material properties used for the different components are
 824 as per the values tabulated in Table 4 of ref. Baghani et al.
 825 (2012), which are different from the material properties
 826 reported in the experiments. This analysis was carried out
 827 to demonstrate that the current formulation can identify and
 828 mimic the nature of stress-strain evolution as observed in
 829 experimental results.

830 Figure 27d shows the free strain recovery for different
 831 amounts of fixed pre-strains with increase in temperature.
 832 As the temperature is increased, the amount of strains
 833 stored in the SMP sample decreases and the structure
 834 comes back to its initial configuration. It can be observed
 835 that even for different types of deformations, the paths
 836 followed during the recovery process are similar. The results
 837 obtained by the current implementation closely resemble

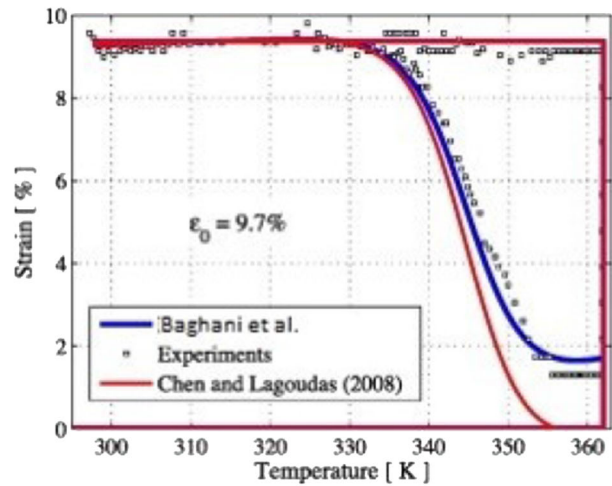
the experimental results as shown in Fig. 27c. These results
 show that the current finite-element implementation can
 correctly capture the time-independent nature of the stress
 and strain evolution for a SMP material.

3.2 Time-dependent SMP behavior

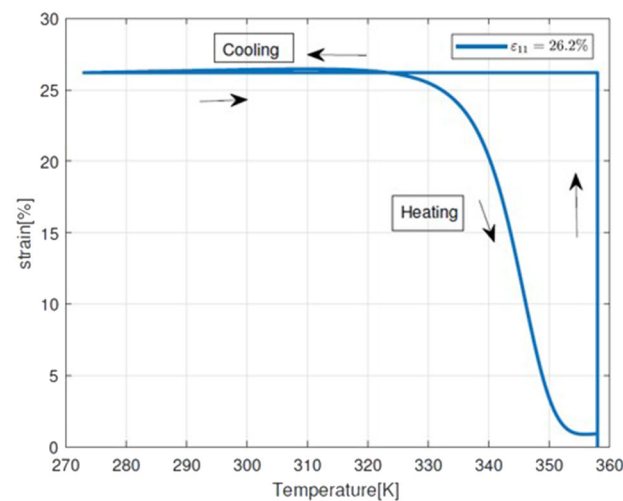
The experiment performed by Li and Nettles (2010) was
 computationally simulated to validate the time-dependent
 aspect of the current implementation. Here, an SMP-based
 foam was compressed under a constant stress, held for 30
 min and was subjected to the thermo-mechanical cycle. The
 main objective is to analyze the nature and form of the
 strain-time behavior. A comparison of the results of the
 current implementation with the numerical studies reported
 by Baghani et al. (2012) is shown in Fig. 28. Note that the



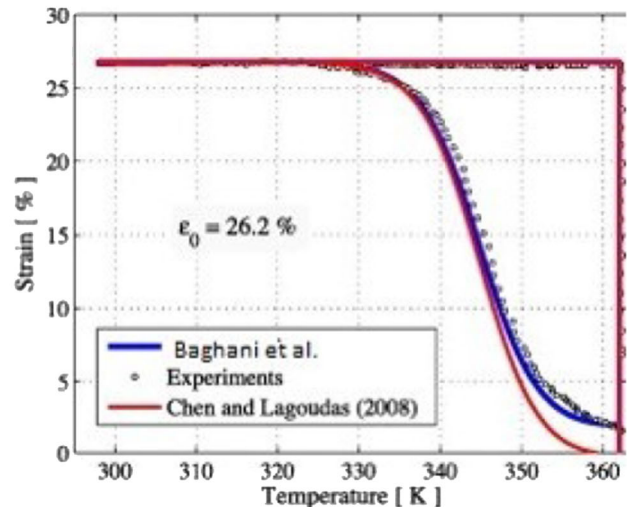
(a)



(b)



(c)



(d)

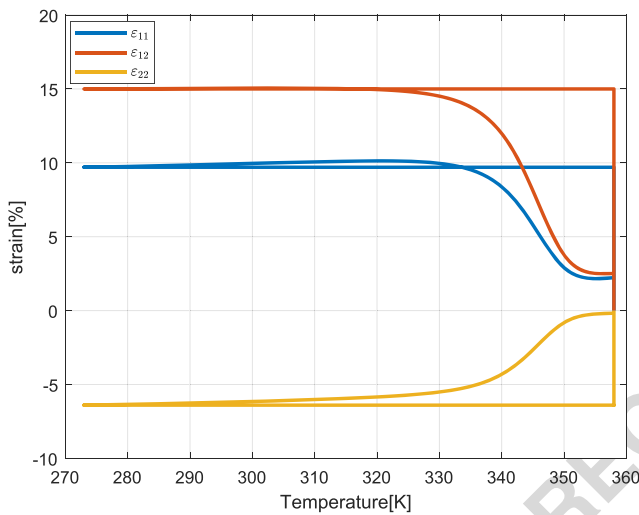
Fig. 29 a, c SMP simulation for uniaxial tensile strain of 9.7% and 26.2% respectively. b, d Experiments reported by Volk et al. (2010) (dotted data points), numerical implementation of Chen and Lagoudas (2008b) and Baghani et al. (2012)

852 deviations observed in Fig. 28a from those in Fig. 28b are
 853 mainly due to the use of different thermal strain function.
 854 We have used the function of thermal strain as given by
 855 (8) to maintain a continuity in our implementation. Also,
 856 the material parameters used differ in the two cases since
 857 we have not included any hard phase. Since our objective
 858 was to show that the current implementation sufficiently
 859 captures the SMP mechanics fit for moving forward with
 860 the topology optimization design, we can conclude that the
 861 overall correlation between the experimental results and the
 862 current implementation agrees to a level sufficient for our
 863 implementation.

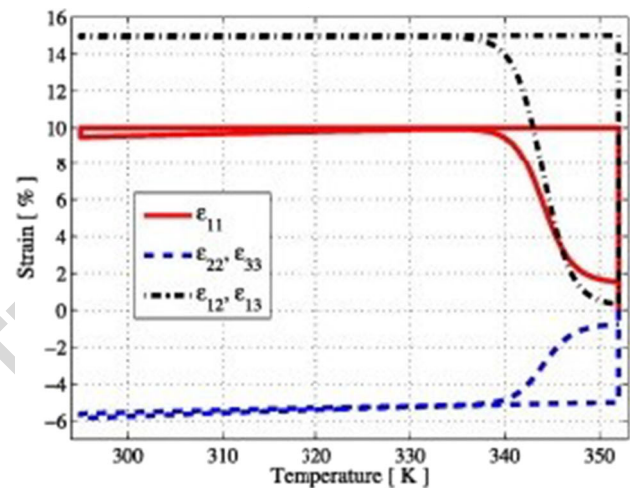
864 Figure 29 compares the current implementation with the
 865 experiments reported by Volk et al. (2010) regarding the

time-dependent uniaxial loading of SMPs followed by the
 thermo-mechanical cycle. We also compare our results with
 the implementation of Baghani et al. (2012). The results
 show that the current implementation can successfully
 capture the time-dependent effects with a moderate level of
 irreversible strains. From Fig. 29, we can observe that the
 strain at $T = T_H$ is not 0, i.e., we do not recover all the strain
 that is put into the structure while it is deformed. This is due
 to the fact that while applying deformation a part of the total
 strain, irreversible strain component(ϵ^i), is permanently lost
 and cannot be recovered.

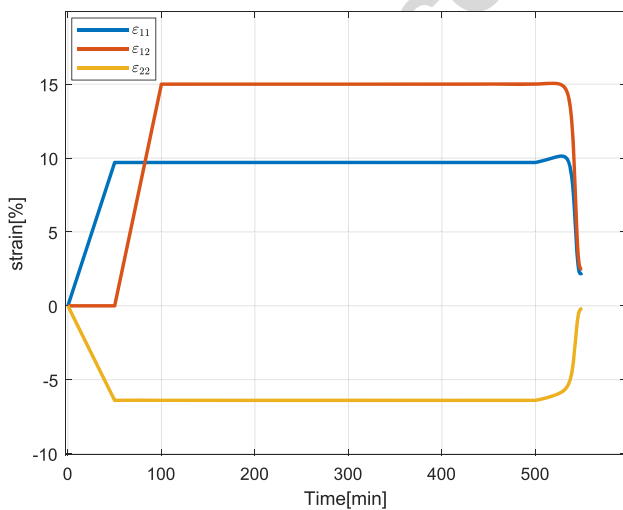
Figure 30 contains results from simulation of the
 multiaxial loading of an SMP material and compares the
 temperature vs. strain and time vs. strain plots obtained



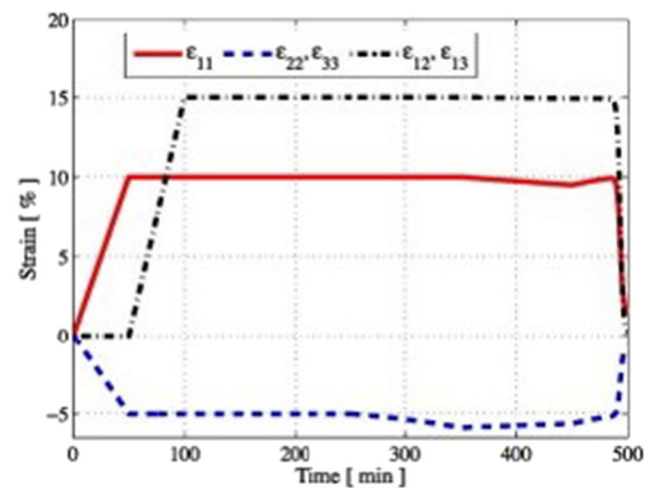
(a)



(b)



(c)



(d)

Fig. 30 a, c Results captured by the current implementation. b, d Simulation results reported by Baghani et al. (2012) for multiaxial loading of an SMP material

880 from the current implementation with the results reported by
 881 Baghani et al. (2012). The similarity of the results indicates
 882 that the current implementation can successfully capture the
 883 multiaxial loading of SMPs.

884 Having verified that the current finite element implementa-
 885 tion of the constitutive model proposed by Baghani et al.
 886 (2012) can capture the essential characteristics of SMPs to
 887 an acceptable level of accuracy, we move forward with the
 888 computational design aspect using topology optimization.

889 **Appendix 4: The symmetry assumption**

890 The results in Section 6.2 assume a symmetric design due to
 891 the symmetry of the loading and boundary conditions.
 892 To verify the assumption, we have also solved the
 893 problem using the full domain. Figure 32 shows the
 894 optimized material distribution for the self-actuating gripper
 895 corresponding to the full-design domain as shown in
 896 Fig. 31a without the assumption of symmetry.

897 The optimization problem statement for the full-domain
 898 case is written as:

$$\begin{aligned} & \underset{\rho}{\text{minimize}} && -(U_y^b - U_y^t)|_{t=T^*} \\ & \text{subject to} && V_{SMP1}(\rho) \leq V_{SMP1}^{Max}, \quad 0 \leq \rho \leq 1 \quad (D.1) \end{aligned}$$

899 The optimized value of U_y^N for the same node and under
 900 the same loading conditions is 2.2758 mm, in the negative y-
 901 direction. If we compare the optimized material distribution
 902 for the half-domain case as shown in Fig. 14 and the full-
 903 domain case as shown in Fig. 32, we observe that the two

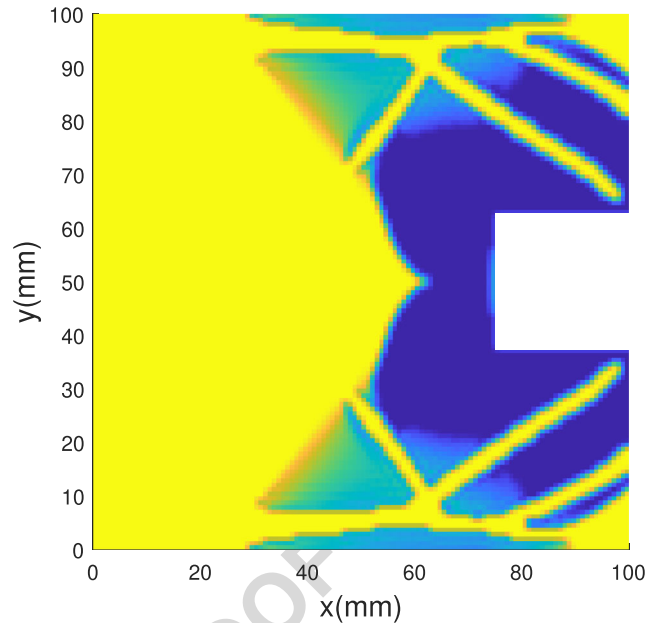


Fig. 32 Optimized material distribution for the self-actuating gripper for the full-design domain

904 results have very similar topologies, with minor differences
 905 in the material distributions. The differences between the
 906 two solutions can be explained by the nonconvex nature
 907 of the optimization problem, which makes the optimization
 908 solutions dependent on both the starting point (initial guess)
 909 of the optimization, the search path followed to arrive at the
 910 final solution.

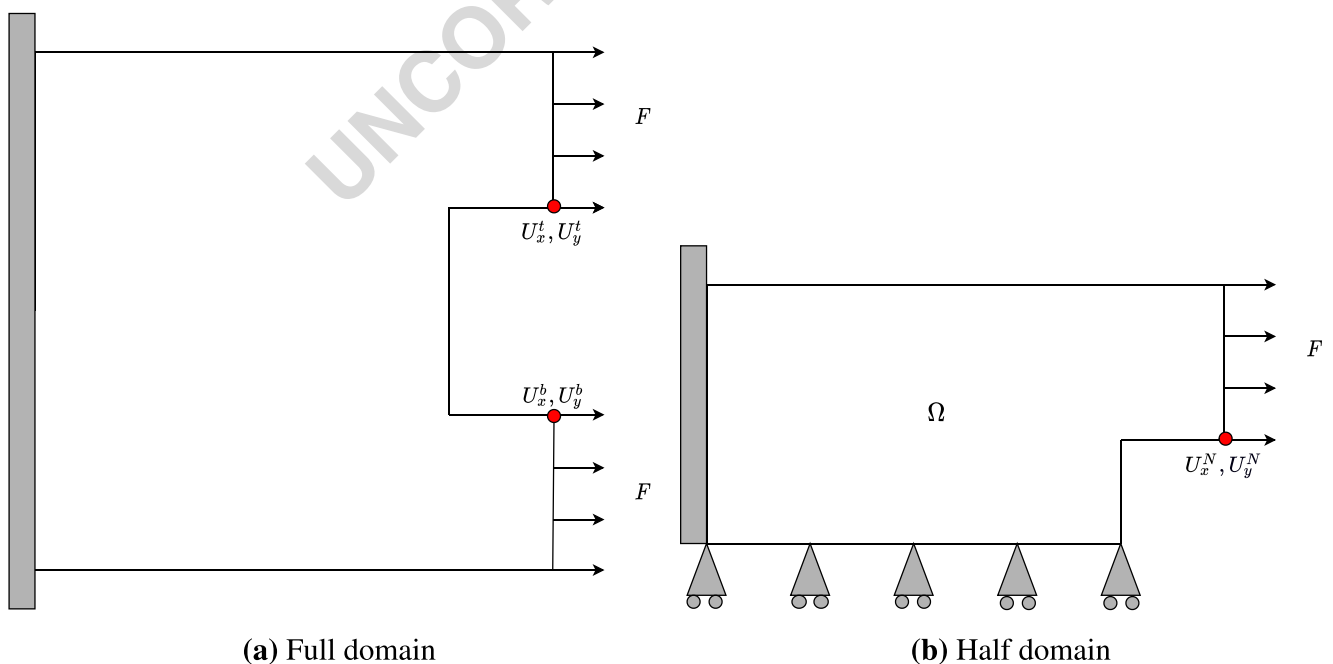


Fig. 31 Boundary conditions for the gripper optimization problem with full and half domains

911 **References**

- 912 Aage N, Andreassen E, Lazarov BS (2015) Topology optimization
913 using PETSc: an easy-to-use, fully parallel, open source topology
914 optimization framework. *Struct Multidiscip Optim* 51(3):565–572
- 915 Baghani M, Naghdabadi R, Arghavani J, Sohrabpour S (2012) A
916 thermodynamically-consistent 3D constitutive model for shape
917 memory polymers. *Int J Plast* 35:13–30. [Online]. Available:
918 [http://www.sciencedirect.com/science/article/pii/S074964191200](http://www.sciencedirect.com/science/article/pii/S0749641912000083)
919 [0083](http://www.sciencedirect.com/science/article/pii/S0749641912000083)
- 920 Behl M, Lendlein A (2011) Shape-memory polymers, pp. 1–16. American
921 Cancer Society, [Online]. Available: [https://onlinelibrary.](https://onlinelibrary.wiley.com/doi/abs/10.1002/0471238961.1908011612051404.a01.pub2)
922 [wiley.com/doi/abs/10.1002/0471238961.1908011612051404.a01.](https://onlinelibrary.wiley.com/doi/abs/10.1002/0471238961.1908011612051404.a01.pub2)
923 [pub2](https://onlinelibrary.wiley.com/doi/abs/10.1002/0471238961.1908011612051404.a01.pub2)
- 924 Bowen CR, Kim HA, Weaver PM, Dunn S (2014) Piezoelectric
925 and ferroelectric materials and structures for energy harvesting
926 applications. *Energy Environ Sci* 7:25–44. [Online]. Available:
927 <https://doi.org/10.1039/C3EE42454E>
- 928 Bendsøe MP, Sigmund O (1999) Material interpolation schemes in
929 topology optimization. *Arch Appl Mech* 69(9):635–654. [Online].
930 Available: <https://doi.org/10.1007/s004190050248>
- 931 Bruns TE, Tortorelli DA (2001) Topology optimization of non-linear
932 elastic structures and compliant mechanisms. *Comput Methods*
933 *Appl Mech Eng* 190(26):3443–3459. [Online]. Available: [http://](http://www.sciencedirect.com/science/article/pii/S0045782500002784)
934 www.sciencedirect.com/science/article/pii/S0045782500002784
- 935 Carbonari RC, Silva ECN, Paulino GH (2008) Topology optimization
936 applied to the design of functionally graded piezoelectric bimorph.
937 *AIP Conf Proc* 1:291–296. [Online]. Available: [https://aip.](https://aip.scitation.org/doi/abs/10.1063/1.2896793)
938 [scitation.org/doi/abs/10.1063/1.2896793](https://aip.scitation.org/doi/abs/10.1063/1.2896793)
- 939 Carrell J, Tate D, Wang S, Zhang H-C (2011) Shape memory polymer
940 snap-fits for active disassembly. *J Clean Prod* 19(17):2066–2074.
941 [Online]. Available: [http://www.sciencedirect.com/science/article/](http://www.sciencedirect.com/science/article/pii/S0959652611002393)
942 [pii/S0959652611002393](http://www.sciencedirect.com/science/article/pii/S0959652611002393)
- 943 Chen Y-C, Lagoudas DC (2008a) A constitutive theory for shape
944 memory polymers. Part I: large deformations. *J Mech Phys Solids*
945 56(5):1752–1765. [Online]. Available: [http://www.sciencedirect.](http://www.sciencedirect.com/science/article/pii/S0022509607002323)
946 [com/science/article/pii/S0022509607002323](http://www.sciencedirect.com/science/article/pii/S0022509607002323)
- 947 Chen Y-C, Lagoudas DC (2008b) A constitutive theory for
948 shape memory polymers. Part II: a linearized model for
949 small deformations. *J Mech Phys Solids* 56(5):1766–1778.
950 [Online]. Available: [http://www.sciencedirect.com/science/article/](http://www.sciencedirect.com/science/article/pii/S0022509607002311)
951 [pii/S0022509607002311](http://www.sciencedirect.com/science/article/pii/S0022509607002311)
- 952 Cho J-H, Azam A, Gracias DH (2010) Three dimensional nanofabrica-
953 tion using surface forces. *Langmuir* 26(21):16534–16539. pMID:
954 20507147. [Online]. Available: <https://doi.org/10.1021/la1013889>
- 955 Choi M-J, Cho S (2018) Isogeometric configuration design opti-
956 mization of shape memory polymer curved beam structures
957 for extremal negative Poisson's ratio. *Struct Multidiscip Optim*
958 58(5):1861–1883. [Online]. Available: [https://doi.org/10.1007/s00](https://doi.org/10.1007/s00158-018-2088-y)
959 [158-018-2088-y](https://doi.org/10.1007/s00158-018-2088-y)
- 960 Frecker MI (2003) Recent advances in optimization of smart structures
961 and actuators. *J Intell Mater Syst Struct* 14(4–5):207–216.
962 [Online]. Available: <https://doi.org/10.1177/1045389X03031062>
- 963 Gaynor AT, Meisel NA, Williams CB, Guest JK (2014) Multiple-
964 material topology optimization of compliant mechanisms
965 created via polyjet three-dimensional printing. *J Manuf*
966 *Sci Eng* 136(6):061015–061015–10. [Online]. Available:
967 <https://doi.org/10.1115/1.4028439>
- 968 Ge Q, Dunn CK, Qi HJ, Dunn ML (2014) Active origami by 4D
969 printing. *Smart Mater Struct* 23(9):094007
- 970 Ge Q, Sakhaei AH, Lee H, Dunn CK, Fang NX, Dunn ML
971 (2016) Multimaterial 4D printing with tailorable shape mem-
972 ory polymers. *Sci Rep* 6:31110 EP. [Online]. Available:
973 <https://doi.org/10.1038/srep31110>
- Geiss MJ, Maute K (2018) Topology optimization of active structures
974 using a higher-order level-set-XFEM-density approach. In: 2018
975 Multidisciplinary analysis and optimization conference, p 4053
976
- Geiss MJ, Boddeti N, Weeger O, Maute K, Dunn ML (2019)
977 Combined level-set-XFEM-density topology optimization of four-
978 dimensional printed structures undergoing large deformation. *J*
979 *Mech Des* 5:141
980
- James KA, Waisman H (2015) Topology optimization of viscoelastic
981 structures using a time-dependent adjoint method. *Comput*
982 *Methods Appl Mech Eng* 285:166–187. [Online]. Available: [http://](http://www.sciencedirect.com/science/article/pii/S004578251400437X)
983 www.sciencedirect.com/science/article/pii/S004578251400437X
984
- Langelaar M, van Keulen F (2008) Modeling of shape memory alloy
985 shells for design optimization. *Comput Struct* 86(9):955–963
986
- Langelaar M, Yoon GH, Kim Y, Van Keulen F (2011) Topology
987 optimization of planar shape memory alloy thermal actuators using
988 element connectivity parameterization. *Int J Numer Methods Eng*
989 88(9):817–840
990
- Lendlein A, Jiang H, Jünger O, Langer R (2005) Light-induced
991 shape-memory polymers. *Nature* 434(7035):879–882. [Online].
992 Available: <https://doi.org/10.1038/nature03496>
993
- Leng J, Yu K, Liu Y (2010) Recent progress of smart composite material
994 in HIT. [Online]. Available: <https://doi.org/10.1117/12.854803>
995
- Li G, Nettles D (2010) Thermomechanical characterization of a shape
996 memory polymer based self-repairing syntactic foam. *Polymer*
997 51(3):755–762. [http://www.sciencedirect.com/science/article/pii/](http://www.sciencedirect.com/science/article/pii/S0032386109010672)
998 [S0032386109010672](http://www.sciencedirect.com/science/article/pii/S0032386109010672)
999
- Liu Y, Gall K, Dunn ML, Greenberg AR, Diani J (2006) Ther-
1000 momechanics of shape memory polymers: uniaxial experi-
1001 ments and constitutive modeling. *Int J Plast* 22(2):279–313.
1002 [Online]. Available: [http://www.sciencedirect.com/science/article/](http://www.sciencedirect.com/science/article/pii/S0749641905000604)
1003 [pii/S0749641905000604](http://www.sciencedirect.com/science/article/pii/S0749641905000604)
1004
- Liu Y, Du H, Liu L, Leng J (2014) Shape memory polymers
1005 and their composites in aerospace applications: a review. *1006*
1007 *Smart Mater Struct* 23(2):023001. [Online]. Available:
1008 <https://doi.org/10.1088/0964-1726/23/2/F023001>
1009
- Maute K, Tkachuk A, Wu J, Jerry Qi H, Ding Z, Dunn
1010 ML (2015) Level set topology optimization of printed active
1011 composites. *J Mech Des* 2015(11):10. [Online]. Available:
1012 <https://doi.org/10.1115/1.4030994>
1013
- Oliver K, Seddon A, Trask RS (2016) Morphing in nature and beyond:
1014 a review of natural and synthetic shape-changing materials
1015 and mechanisms. *J Mater Sci* 51(24):10663–10689. [Online].
1016 Available: <https://doi.org/10.1007/s10853-016-0295-8>
1017
- Qi HJ, Nguyen TD, Castro F, Yakacki CM, Shandas R (2008) Finite
1018 deformation thermo-mechanical behavior of thermally induced
1019 shape memory polymers. *J Mech Phys Solids* 56(5):1730–1751.
1020 [Online]. Available: [http://www.sciencedirect.com/science/article/](http://www.sciencedirect.com/science/article/pii/S002250960700230X)
1021 [pii/S002250960700230X](http://www.sciencedirect.com/science/article/pii/S002250960700230X)
1022
- Reed JL Jr, Hemmelgarn CD, Pelley BM, Havens E (2005) Adaptive
1023 wing structures. [Online]. Available: [https://doi.org/10.1117/12.59](https://doi.org/10.1117/12.599922)
1024 [9922](https://doi.org/10.1117/12.599922)
- Reese S, Böl M, Christ D (2010) Finite element-based multi-
1025 phase modelling of shape memory polymer stents. *Comput*
1026 *Methods Appl Mech Eng* 199(21):1276–1286. Multiscale mod-
1027 els and mathematical aspects in solid and fluid mechanics.
1028 [Online]. Available: [http://www.sciencedirect.com/science/article/](http://www.sciencedirect.com/science/article/pii/S004578250900262X)
1029 [pii/S004578250900262X](http://www.sciencedirect.com/science/article/pii/S004578250900262X)
1030
- Rupp CJ, Evgrafov A, Maute K, Dunn ML (2009) Design
1031 of piezoelectric energy harvesting systems: a topology opti-
1032 mization approach based on multilayer plates and shells. *J*
1033 *Intell Mater Syst Struct* 20(16):1923–1939. [Online]. Available:
1034 <https://doi.org/10.1177/1045389X09341200>
1035
- Svanberg K (1987) The method of moving asymptotes—a new method
1036 for structural optimization. *Int J Numer Methods Eng* 24(2):359–
1037

- 1038 373. [Online]. Available: [https://onlinelibrary.wiley.com/doi/abs/](https://onlinelibrary.wiley.com/doi/abs/10.1002/nme.1620240207)
1039 [10.1002/nme.1620240207](https://onlinelibrary.wiley.com/doi/abs/10.1002/nme.1620240207)
- 1040 Siéfert E, Reyssat E, Bico J, Roman B (2019) Bio-inspired pneumatic
1041 shape-morphing elastomers. *Nat Mater* 18(1):24–28. [Online].
1042 Available: <https://doi.org/10.1038/s41563-018-0219-x>
- 1043 Sigmund O, Torquato S (1999) Design of smart composite materials
1044 using topology optimization. *Smart Mater Struct* 8(3):365–379.
1045 [Online]. Available: [https://doi.org/10.1088%2F0964-1726%2F8](https://doi.org/10.1088%2F0964-1726%2F8%2F3%2F308)
1046 [%2F3%2F308](https://doi.org/10.1088%2F0964-1726%2F8%2F3%2F308)
- 1047 Silva ECN, Kikuchi N (1999) Design of piezoelectric transducers
1048 using topology optimization. *Smart Mater Struct* 8(3):350–364.
1049 [Online]. Available: [https://doi.org/10.1088%2F0964-1726%2F8](https://doi.org/10.1088%2F0964-1726%2F8%2F3%2F307)
1050 [%2F3%2F307](https://doi.org/10.1088%2F0964-1726%2F8%2F3%2F307)
- 1051 Tibbits S (2014) 4D printing: multi-material shape change. *Archit Des*
1052 84(1):116–121. [Online]. Available: [https://onlinelibrary.wiley.](https://onlinelibrary.wiley.com/doi/abs/10.1002/ad.1710)
1053 [com/doi/abs/10.1002/ad.1710](https://onlinelibrary.wiley.com/doi/abs/10.1002/ad.1710)
- 1054 Volk BL, Lagoudas DC, Chen Y-C, Whitley KS (2010) Analysis of the
1055 finite deformation response of shape memory polymers: I. Ther-
1056 momechanical characterization. *Smart Mater Struct* 19(7):075005
- Volk BL, Lagoudas DC, Maitland DJ (2011) Characterizing and
1057 modeling the free recovery and constrained recovery behavior
1058 of a polyurethane shape memory polymer. *Smart Mater Struct*
1059 20(9):094004. [Online]. Available: [https://doi.org/10.1088%2F09](https://doi.org/10.1088%2F0964-1726%2F20%2F9%2F094004)
1060 [64-1726%2F20%2F9%2F094004](https://doi.org/10.1088%2F0964-1726%2F20%2F9%2F094004)
1061
- Wache HM, Tartakowska DJ, Hentrich A, Wagner MH (2003)
1062 Development of a polymer stent with shape memory effect as a
1063 drug delivery system. *J Mater Sci: Mater Med* 14(2):109–112.
1064 [Online]. Available: <https://doi.org/10.1023/A:1022007510352>
1065
- Yin L, Ananthasuresh G (2002) A novel topology design scheme for
1066 the multi-physics problems of electro-thermally actuated com-
1067 pliant micromechanisms. *Sens Actuat A: Phys* 97–98:599–609.
1068 Selected papers from Eurosenors XV. [Online]. Available: [http://](http://www.sciencedirect.com/science/article/pii/S0924424701008536)
1069 www.sciencedirect.com/science/article/pii/S0924424701008536
1070
- Yu K, Yin W, Sun S, Liu Y, Leng J (2009) Design and analysis of
1071 morphing wing based on SMP composite. [Online]. Available:
1072 <https://doi.org/10.1117/12.815712>
1073
- Publisher's note** Springer Nature remains neutral with regard to
1074 jurisdictional claims in published maps and institutional affiliations. 1075

UNCORRECTED PROOF